

# P-block element modulated 1 T phase MoS<sub>2</sub> with Ru lattice grafting for high-performance Li||O<sub>2</sub> batteries

Received: 18 October 2023

Accepted: 27 November 2024

Published online: 07 February 2025



Peng Wang<sup>1</sup> , Danyang Zhao<sup>1</sup>, Peng Zhang<sup>1</sup>, Xiaobin Hui<sup>1,2</sup>, Zhiwei Zhang<sup>1</sup> ,  
Rutao Wang<sup>1</sup> , Chengxiang Wang<sup>1</sup>, Xiaoli Ge<sup>1,3</sup> , Xiaojing Liu<sup>4</sup> ,  
Yuguang C. Li<sup>3</sup>  & Longwei Yin<sup>1</sup> 

The metallic phase MoS<sub>2</sub> (1T-MoS<sub>2</sub>) supported metal-nanocatalyst is an appealing material system for accelerating the redox kinetics of non-aqueous Li||O<sub>2</sub> batteries. However, the drawbacks associated with the surface orbital steric effect and the internal electron coupling results in a detrimental effect for the stability of 1T-MoS<sub>2</sub>, especially for the interface charge transfer. This makes it difficult to incorporate guest metal nanoparticles without compromising the 1 T phase support. To circumvent these issues, here we propose a p-block element (In-O) doping strategy to stabilize the 1 T phase MoS<sub>2</sub> by moderating the surface orbital steric effect and strengthening the internal chemical bonding, and thus for the epitaxial Ru nanocatalyst graft on the stabilized 1T-MoS<sub>2</sub> for Li||O<sub>2</sub> batteries. The experimental and theoretical analyzes indicate that the In-O-MoS<sub>2</sub>@Ru enhances the O<sub>2</sub> dissociation and facilitates the adsorption of LiO<sub>2</sub> intermediates. This effect promotes the growth of weakly crystalline Li<sub>2</sub>O<sub>2</sub> films during oxygen reduction reaction, which can be more easily decomposed during the oxygen evolution reaction, thereby enhancing the bifunctional-catalytic kinetics. When employed at the positive electrode for non-aqueous Li||O<sub>2</sub> batteries, In-O-MoS<sub>2</sub>@Ru shows an overpotential of 0.37 V and a cycling life of 284 cycles at 200 mA g<sup>-1</sup> with a final discharge specific capacity of 1000 mAh g<sup>-1</sup> at 25 °C.

Given the high theoretical specific energy of 3500 Wh kg<sup>-1</sup>, non-aqueous lithium||oxygen (Li||O<sub>2</sub>) batteries demonstrate promising potential industrial applications compared to state-of-the-art lithium-ion battery counterparts<sup>1–3</sup>. However, due to the complex multi-step and multi-electron redox chemistry involved during the oxygen reduction reaction (ORR) and oxygen evolution reaction (OER), both the mass transfer and surface reaction kinetics are usually sluggish. Furthermore, the intrinsically insulating

characteristics and insolubility of the solid discharge product, Li<sub>2</sub>O<sub>2</sub>, contribute to large over-potential<sup>4–6</sup>. The electrochemical performance of the catalytic positive electrode is closely associated with the growth and decomposition behaviors of Li<sub>2</sub>O<sub>2</sub><sup>7</sup>. Therefore, the focus of Li||O<sub>2</sub> battery research is centered on developing an efficient catalyst to modulate the nucleation-growth of Li<sub>2</sub>O<sub>2</sub> during ORR and facilitate its rapid decomposition during OER<sup>8,9</sup>.

<sup>1</sup>Key Laboratory for Liquid-Solid Structural Evolution and Processing of Materials, Ministry of Education, School of Materials Science and Engineering, Shandong University, Jinan, P.R. China. <sup>2</sup>The Hong Kong Polytechnic University, Yuk Choi Road No. 11, Hung Hom, Kowloon, Hong Kong. <sup>3</sup>Department of Chemistry, State University of New York at Buffalo, Buffalo, New York, USA. <sup>4</sup>Institute of Frontier Chemistry, School of Chemistry and Chemical Engineering, Shandong University, Qingdao, P.R. China. ✉e-mail: [zhangzhiwei@sdu.edu.cn](mailto:zhangzhiwei@sdu.edu.cn); [Rtwang@sdu.edu.cn](mailto:Rtwang@sdu.edu.cn); [xiaoli@buffalo.edu](mailto:xiaoli@buffalo.edu); [liuxj2020@sdu.edu.cn](mailto:liuxj2020@sdu.edu.cn); [yinlw@sdu.edu.cn](mailto:yinlw@sdu.edu.cn)

Transition metal compounds supported noble metals (Ru, Pt) nanocatalysts have been proven to be effective catalysts for  $\text{Li}||\text{O}_2$  batteries due to their rich interfacial active sites and robust metal-support interaction. Notably, molybdenum disulfide ( $\text{MoS}_2$ ) is widely applied due to its low cost and layer interval controllability<sup>10–14</sup>. Compared to the semiconducting 2H phase, the metallic 1T phase  $\text{MoS}_2$  exhibits enhanced electrocatalytic efficiency<sup>15–24</sup>. Therefore, the 1T  $\text{MoS}_2$  is often preferred as the host matrix to confine the guest metal-nanoparticles. However, the vertically unoccupied  $\sigma^*$  antibonding orbital near the Fermi level of 1T- $\text{MoS}_2$  has a favorable steric orientation to facilitate the interface charge transfer (Supplementary Fig. 1a), and the bonding between Mo  $sp^3d^2$  hybrid orbitals and the S nonequivalent  $sp^3$  hybrid orbitals in the octahedral unit of 1T- $\text{MoS}_2$  only have a single  $\sigma$  bonding delocalization for electronic coupling (Supplementary Fig. 1b), both of which implies inherent instability for the electrochemical reaction with strong interfacial charge transfer. Consequently, when combined with guest metals, the vertical unoccupied  $\sigma^*$  antibonding orbital of 1T- $\text{MoS}_2$  becomes susceptible to electron filling. This will further reduce the initially insufficient electronic coupling strength, and potentially compromising the 1T phase structure. As a result, achieving controlled growth of guest metal nanoparticles at the interface while maintaining the stabilized 1T  $\text{MoS}_2$  structure remains a significant challenge. However, there are limited reports on hybrid material comprising of 1T  $\text{MoS}_2$  and supported metal nanoparticles.

Herein, we propose a strategy to modulate 1T phase  $\text{MoS}_2$  with In-O doping and lattice-grafting of Ru. The atomically doped p-block In-O can effectively reduce the distribution of vertical orbitals, enhancing the inherent bonding strength within In-O- $\text{MoS}_2$  and contributing to the stabilization of the 1T  $\text{MoS}_2$ . The lattice matching provided by In-O co-doping facilitates the epitaxial growth of Ru nanocrystals along the lattice of In-O- $\text{MoS}_2$ . The In-O- $\text{MoS}_2$ @Ru hetero-interface with low-angle torsion provides rich accessible catalytic active sites. The local charge rearrangement and electronic structure optimization lead to enhanced O-O cleavage capability and  $\text{LiO}_2$  intermediate adsorption characteristic. Notably, this In-O- $\text{MoS}_2$ @Ru catalyst demonstrates good bifunctionally-catalytic ORR/OER kinetics in  $\text{Li}||\text{O}_2$  batteries. A low ORR/OER overpotential of only 0.37 V and a much improved life of 284 cycles at 200  $\text{mA g}^{-1}$  can be achieved for the In-O- $\text{MoS}_2$ @Ru based  $\text{Li}||\text{O}_2$  batteries, which is at the top level among the state-of-the-art catalysts ever reported. This material strategy combines p-block element modulated 1T phase  $\text{MoS}_2$  with Ru lattice grafting to achieve high-performance  $\text{Li}||\text{O}_2$  batteries, offering perspectives for the design of bifunctional catalysts.

## Results

### Microstructure characterization

The design strategy for the In-O- $\text{MoS}_2$ @Ru catalyst is illustrated as Fig. 1a. First, In-O doping induced 1T phase  $\text{MoS}_2$  (In-O- $\text{MoS}_2$ ) was fabricated through a facile hydrothermal procedure. During this process, trace oxygen and indium species derived from indium precursors can be simultaneously incorporated into the  $\text{MoS}_2$  lattice and contribute to the formation of 1T  $\text{MoS}_2$  during hydrothermal reaction. Moreover the substitutional doped In atoms are incline to coordinate with neighboring O atoms, constructing In-O-Mo coordination environment in local region of the  $\text{MoS}_2$  substrate. This is considerably different from those reported metal-S bond for transition metals doped  $\text{MoS}_2$ <sup>15–20</sup>. The reason for the choice of In-O doping within  $\text{MoS}_2$  lies in three points. a) As main group metal, In possess more active  $s/p$ -type valence electrons than that of Mo. Based on the molecular orbital theory, the introduction of In atoms into  $\text{MoS}_2$  can form a stronger  $s/p$  electron coupling than the  $d/p$  coupling within  $\text{MoS}_2$ , resulting in a lower bonding orbital and higher antibonding orbital and thus benefiting the inherent stability. And what's more, the O element possesses the same valence electron number with S. Specially, due to lower

energy  $2p$  valence electrons and smaller atomic radius of O than that of S, partially substituting S with O could further exacerbate the nonequivalence of  $sp^3$  hybridization. This consequently enhances the inherent electronic coupling and stability. b) Because the ionic radius of indium (0.081 nm) is larger than that of molybdenum (0.065 nm), the substitutional doping of indium at molybdenum site within  $\text{MoS}_2$  contributes to producing defect sites. c) The p-block metal functionalized  $\text{MoS}_2$  as efficient catalyst is highly expected but still in its infancy. Then by virtue of In-O mediation within  $\text{MoS}_2$ , Ru nanoparticles are be intimately immobilized within the lattice of In-O- $\text{MoS}_2$  matrix via a grafting-growth strategy, which will construct a stable epitaxial hetero-interface without damage of 1T phase support. The grafting of Ru nanocrystals on In-O- $\text{MoS}_2$  is related to the following three key factors. First, the same hexagonal crystal structure of Ru and  $\text{MoS}_2$  could facilitates the epitaxial growth of Ru nanoparticle on In-O- $\text{MoS}_2$ . Taking consideration on the little lattice mismatch between Ru and  $\text{MoS}_2$ , there exist a small low-angle boundary between Ru and  $\text{MoS}_2$  to relieve the lattice stress. Second, the intense electronic interaction between Ru and O provides additional opportunities for confining guest Ru nanoparticle by stable covalent Ru-O bonding and thus contributing to strengthening the metal-support connect. Thirdly, the In-O doping within the  $\text{MoS}_2$  matrix exposed lattice defects provides abundant potential sites for the following nucleation and growth of the guest Ru nanoparticles.

The surface atomic arrangement and interfacial atomic configuration of In-O- $\text{MoS}_2$ @Ru are identified by electron microscopy. The scanning electron microscopy (SEM) image in Fig. 1b shows that the In-O- $\text{MoS}_2$ @Ru catalyst keeps a nano-flower morphology composed of ultrathin curly nanosheets, offering a large specific area of 78.3  $\text{m}^2 \text{g}^{-1}$  (Supplementary Fig. 2). It suggests that this well-designed catalyst with hierarchical porous structure is beneficial for high exposure of the catalytic centers, fully wetting of electrolyte and efficient optimization of the three-phase interface during long-term ORR/OER cycling. The transmission electron microscopy (TEM) image in Fig. 1c shows the Ru nanoparticles, with an average size of 4 nm, are uniformly distributed within the In-O- $\text{MoS}_2$ , indicating the In-O- $\text{MoS}_2$  host can suppress the aggregation of Ru nanoparticles. As shown in the high-angle annular dark-field scanning transmission electron microscopy (HAADF-STEM) image of the enlarged In-O- $\text{MoS}_2$  matrix part of In-O- $\text{MoS}_2$ @Ru in Fig. 1d, according to atomic number induced brightness contrast between Mo and In atoms, the brighter spots marked by red circles are assigned to the doped In atoms. Figure 1e shows the relative intensity profiles obtained from Line 1 and 2 in Fig. 1d, which further verify that in comparison to Mo atoms, heavier In atoms appear with stronger intensity, indicating In atoms are successfully doped into  $\text{MoS}_2$  lattice and occupy the Mo sites. More importantly, two sulfur atoms can be observed between adjacent molybdenum atoms, and the intensity ratio between sulfur and molybdenum sites is about 0.1–0.2 (Fig. 1e), which is the typical proofs for the presence of 1T  $\text{MoS}_2$ <sup>25</sup>. Then the 3D intensity profile in Fig. 1f (captured from Fig. 1d) also supports the presence of In atoms within  $\text{MoS}_2$  matrix. It should be noted that after decoration of the Ru nanoparticles, the 1T phase remains intact. This indicates that the introduction of the In-O atoms and their atomic-scale distribution exert crucial influence on the formation and stabilization of 1T phase  $\text{MoS}_2$  with octahedral coordination geometry (Fig. 1g). This assertion is further evidenced from the X-ray photoelectron spectroscopy (XPS) and Raman results discussed later.

Furthermore, the high resolution TEM (HRTEM) result in Fig. 2a indicates the continuous lattice fringes across the hetero-interface within In-O- $\text{MoS}_2$ @Ru with an epitaxial growth relation. The high resolution HAADF-STEM image in Fig. 2b further confirms a well-defined host-guest interface between Ru nanoparticles and In-O- $\text{MoS}_2$ . Importantly, Ru nanoparticles have been successfully integrated along the lattice of In-O- $\text{MoS}_2$ , giving rise to a lattice-grafted 0D/2D hetero-structure. In addition, as shown in the magnified image of the In-O-

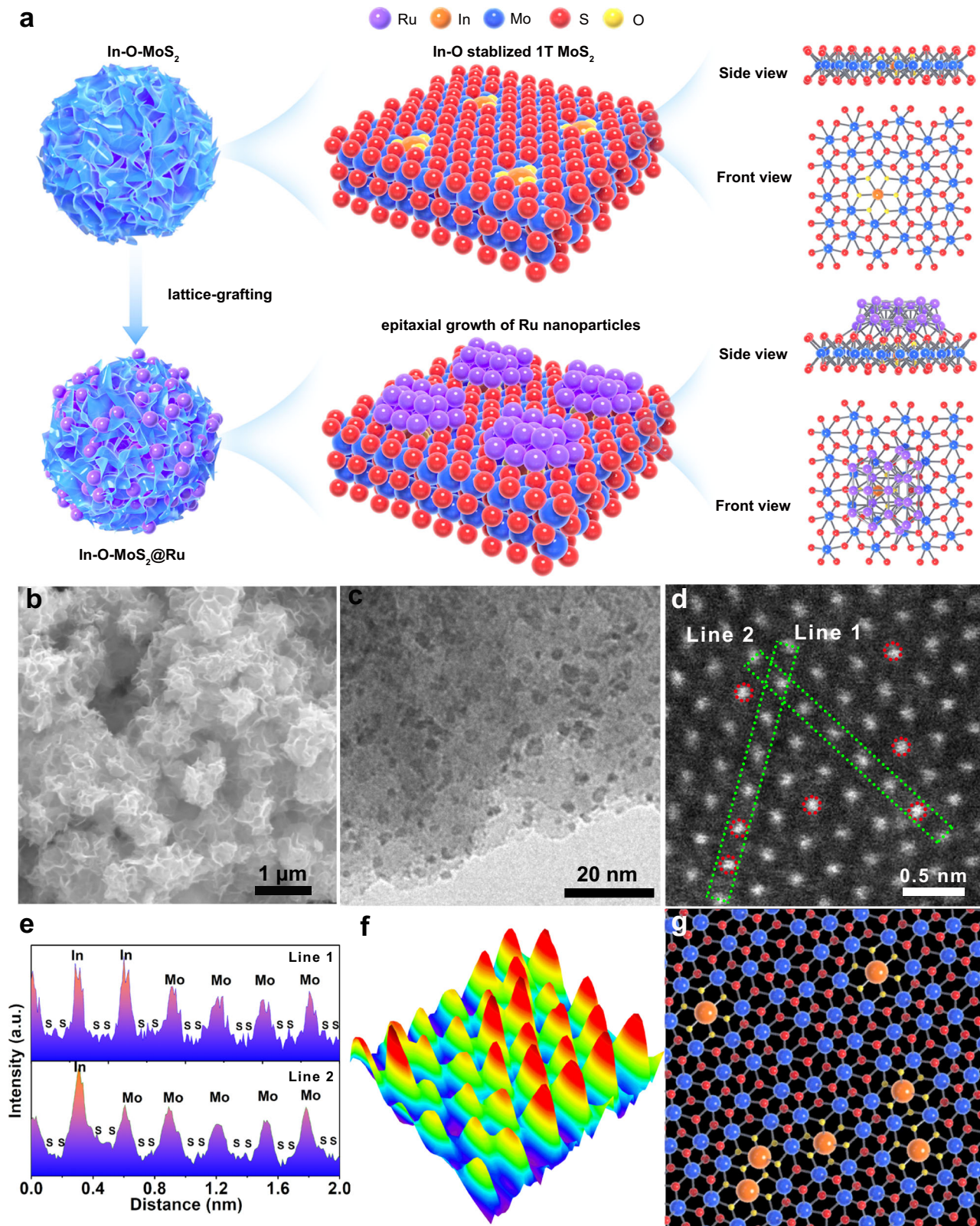


**Fig. 1 | Synthesis, morphology, and structure of In-O-MoS<sub>2</sub>@Ru.** The Mo, S, Ru, In and O atoms are described by blue, red, purple, orange and yellow balls, respectively. **a** Schematic illustration for synthesis of In-O-MoS<sub>2</sub>@Ru. **b** SEM image of In-O-MoS<sub>2</sub>@Ru. **c** Bright-field TEM image of In-O-MoS<sub>2</sub>@Ru. **d** High-angle annular dark-field STEM image of In-O-MoS<sub>2</sub> substrate in In-O-MoS<sub>2</sub>@Ru.

**e** Intensity profile of two different areas captured from Fig. 1d, a. u. stands for arbitrary units in this work. **f** 3D intensity profile captured from Fig. 1d. **g** Schematic illustration of In-O-MoS<sub>2</sub> substrate in In-O-MoS<sub>2</sub>@Ru according to Fig. 1d. Source data are provided as a Source Data file.



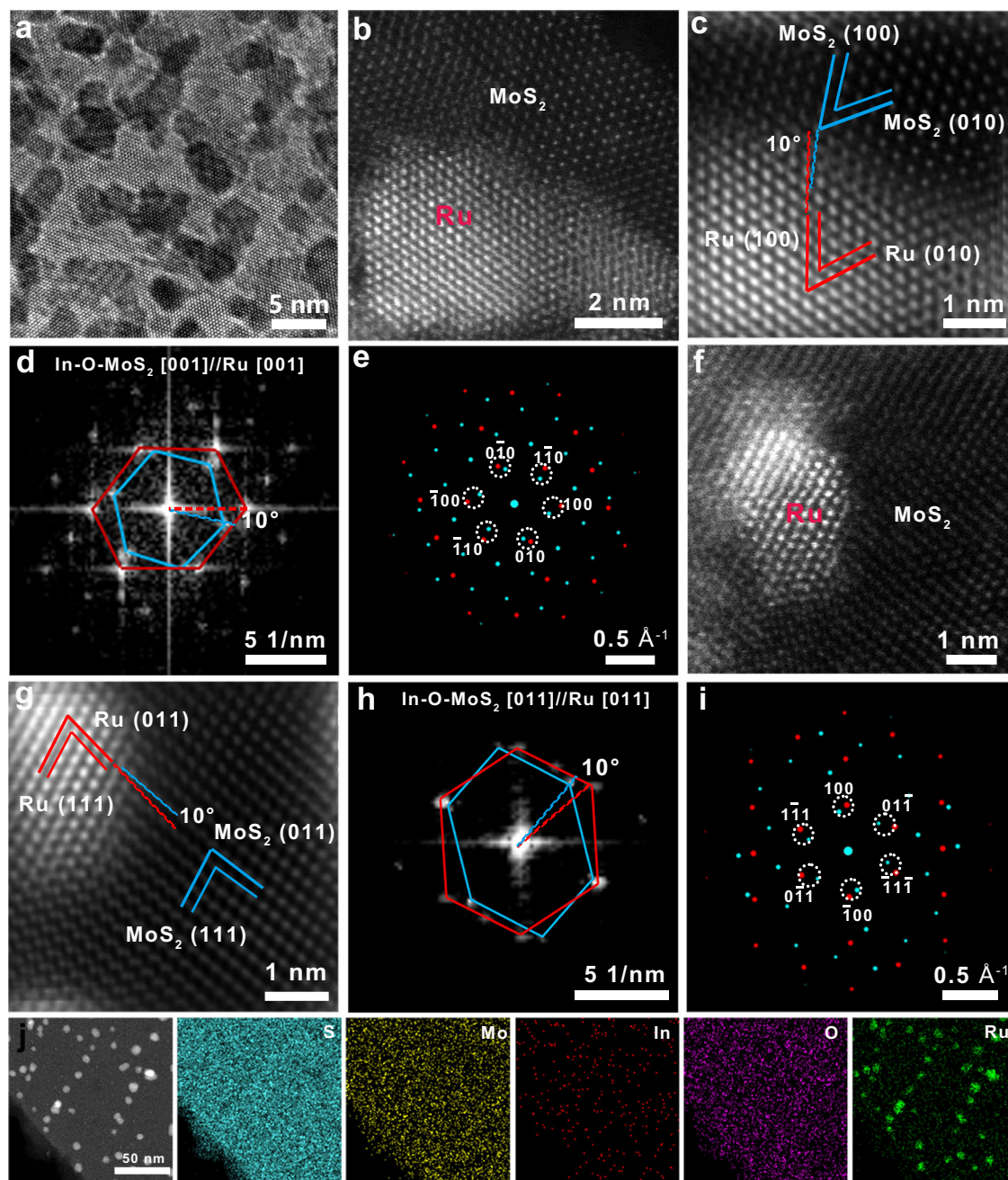


**Fig. 2 | TEM and HAADF-STEM images of In-O-MoS<sub>2</sub>@Ru.** **a** Bright-field HRTEM image of In-O-MoS<sub>2</sub>@Ru. **b** High-angle annular dark-field STEM image of In-O-MoS<sub>2</sub>@Ru. **c** Inverse FFT pattern of zoomed-in the high-angle annular dark-field STEM image at the In-O-MoS<sub>2</sub>@Ru interface area in Fig. 2b. **d** FFT patterns of In-O-MoS<sub>2</sub>@Ru for Fig. 2c. **e** The simulated diffraction patterns of Fig. 1d. **f** High-angle

annular dark-field STEM image of In-O-MoS<sub>2</sub>@Ru at another area. **g** Inverse FFT pattern of zoomed-in the high-angle annular dark-field STEM image at the In-O-MoS<sub>2</sub>@Ru interface area in Fig. 2f. **h** FFT patterns of In-O-MoS<sub>2</sub>@Ru for Fig. 2g. **i** The simulated diffraction patterns of Fig. 2h. **j** Element mapping images for In-O-MoS<sub>2</sub>@Ru.

MoS<sub>2</sub>@Ru interface in Fig. 2c, the blue highlighted lattice fringes are indexed to (100) and (010) facets of host MoS<sub>2</sub> and the red highlighted lattice fringes are matched with (100) and (010) facets of guest Ru<sup>26</sup>. This observation confirms the epitaxial growth of Ru nanoparticles along the In-O-MoS<sub>2</sub> lattice. The fast Fourier transformation (FFT) pattern (Fig. 2d) from the In-O-MoS<sub>2</sub>@Ru in Fig. 2c demonstrates two independent sets of spots coexist along the same [001] zone axis, which match well with In-O-MoS<sub>2</sub> (blue lines) and Ru nanoparticles (red lines), respectively. The distinct 10° deviation between the two sets of spots also manifests a low angle boundary around the hetero-interface. The corresponding simulated diffraction patterns in Fig. 2e confirm the calibrated crystal index of (100), (010) and (110) in pairs are

assigned to In-O-MoS<sub>2</sub> and Ru nanoparticles, respectively, revealing a lattice-matched grafting between In-O-MoS<sub>2</sub> and Ru. Due to the slight lattice mismatch, lattice stress is inevitably generated at the closely-contacted interface. This contributes to the formation of low-angle twist between Ru nanoparticles and In-O-MoS<sub>2</sub>. In spite of lattice stress, the two substances demonstrate superior lattice compatibility with the epitaxial orientation at the interface. Therefore, this situation not only enhances the stability of the In-O-MoS<sub>2</sub>/Ru hetero-interface, but also provides additional catalytic activity.

To validate the universality of lattice coherency orientation, another area with different facets was demonstrated. As shown in the HAADF-STEM images of In-O-MoS<sub>2</sub>@Ru (Fig. 2f and g) also confirm the

interfacial lattice compatibility with the epitaxial relationship. Two adjacent lattice fringes with  $d$ -spacing of 2.08 Å and 2.67 Å are indexed into the (011) and (111) planes of Ru nanoparticles and In-O-MoS<sub>2</sub>, respectively. The FFT spots (Fig. 2h) and the corresponding simulated diffraction patterns (Fig. 2i) viewed along another [011] orientation also demonstrate the lattice stress induced low angle boundary of about 10°, which is consistent with Figs. 2d, e. The selected area electron diffraction (SAED) pattern (Supplementary Fig. 3) taken from the zone in Fig. 1a can be indexed into (103), (110) planes of In-O-MoS<sub>2</sub> and (101), (110) planes of Ru, respectively, further confirming the successful preparation of In-O-MoS<sub>2</sub>@Ru hybrid. To further disclose the potential epitaxial growth mechanism of Ru nanoparticles from In-O-MoS<sub>2</sub>, the In-O-MoS<sub>2</sub>@Ru sintered for 0.5 and 1.0 h were also prepared. As shown in the HAADF-STEM image of In-O-MoS<sub>2</sub>@Ru-0.5 h (Supplementary Fig. 4a), abundant Ru ions are first adsorbed at the surface defective sites introduced by In-O co-doping. As shown in the HAADF-STEM image of In-O-MoS<sub>2</sub>@Ru-1.0 h (Supplementary Fig. 4b), many amorphous and weakly crystallized Ru clusters are grown along the lattice of In-O-MoS<sub>2</sub> and stabilized on the substrate. When it comes to In-O-MoS<sub>2</sub>@Ru, due to intense lattice confinement effect between the hexagonal Ru nanocrystals and In-O-MoS<sub>2</sub>, apparent lattice coherency orientations emerge (Fig. 2b-c and Fig. 2f-g). Herein, the stepwise nucleation, crystallization and epitaxial growth mechanism of Ru nanocrystals from the In-O-MoS<sub>2</sub> lattice is schematically demonstrated in Supplementary Fig. 4c. Meanwhile, the corresponding element mapping images of In-O-MoS<sub>2</sub>@Ru in Fig. 2j verify the homogeneous distribution of S, Mo, In, O and Ru elements throughout the whole catalyst surface. Furthermore, according to the inductively coupled plasma optical emission spectrometry (ICP-OES) results, the mass fractions of In and Ru components are determined to be 1.98 wt.% and 16.3 wt.%, respectively. As expected, multiple types of atomic-scale active centers stemmed from phase engineering induced by In-O heteroatom doping and the phase boundary engineering dominated by host-guest lattice compatibility are simultaneously constructed within the In-O-MoS<sub>2</sub>@Ru composite to synergistically tailor the electronic structure of metal centers and surface chemical characteristics. Accordingly, this multiscale metal-support interaction construction strategy can break through the active sites limitation of the inert 2H MoS<sub>2</sub> basal domains and maximize the accessible catalytic centers for both ORR and OER processes.

The X-ray diffraction (XRD) profile of In-O-MoS<sub>2</sub>@Ru (Supplementary Fig. 5) demonstrates distinct diffraction pattern of MoS<sub>2</sub> and Ru nanoparticles (Supplementary Note 1). Raman spectra of In-O-MoS<sub>2</sub> and In-O-MoS<sub>2</sub>@Ru (Supplementary Fig. 6) further confirm the 1T phase MoS<sub>2</sub> with significant peak at 143.7 (J<sub>1</sub>), 218.7 (J<sub>2</sub>) and 340.2 (J<sub>3</sub>) cm<sup>-1</sup> wavenumber<sup>18,25,27</sup>. This indicates the key role of In-O doping in retaining the 1T phase stability (Supplementary Note 2). To validate the critical roles of O-atom doping in grafting Ru nanoparticles, In-MoS<sub>2</sub>@Ru without O-atom doping was fabricated (see “Method” part). As demonstrated in the Raman spectra and TEM image of In-MoS<sub>2</sub>@Ru (Supplementary Fig. 7), the MoS<sub>2</sub> phase is transferred to 2H for In-MoS<sub>2</sub>@Ru, where most of Ru nanoparticles are reasonably confined on the edge region of the nanosheet due to the inferior surface parallel orbital steric orientation of 2H-MoS<sub>2</sub><sup>11</sup>. This clearly indicates that without the medium of O-atom doping, the In-MoS<sub>2</sub> tends to occur phase transfer to 2H and Ru nanoparticles are inclined to grown from edge via the limited coordinatively unsaturated S atoms. The X-ray photoelectron spectroscopy (XPS) spectra can further unravel the effects of In-O doping and Ru coupling on the phase component and electronic structure of In-O-MoS<sub>2</sub>@Ru. As shown in Mo 3*d* high-resolution spectra (Supplementary Fig. 8a), for In-O-MoS<sub>2</sub>@Ru and In-O-MoS<sub>2</sub>, the peaks at 228.5 and 231.6 eV can be attributed to Mo 3*d*<sub>5/2</sub> and Mo 3*d*<sub>3/2</sub> of 1T MoS<sub>2</sub>, respectively, while the peaks of Mo 3*d*<sub>5/2</sub> and Mo 3*d*<sub>3/2</sub> of 2H MoS<sub>2</sub> are shifted up to 229.4 and 232.5 eV, respectively<sup>16,21,28–30</sup>. Clearly, there is distinctly red-shift phenomenon

by about 1 eV for Mo 3*d* peaks of In-O-MoS<sub>2</sub>@Ru and In-O-MoS<sub>2</sub> relative to pure 2H-MoS<sub>2</sub>. This further indicates the In-O co-doping definitely modulates the electronic structure and stabilizes the metallic 1T phase MoS<sub>2</sub> without phase transfer to 2H phase. According to the peak integration area, the 1T phase MoS<sub>2</sub> contents in In-O-MoS<sub>2</sub>@Ru and In-O-MoS<sub>2</sub> are determined as 89.2% and 86.3%, respectively, indicating the domination of high purity 1T MoS<sub>2</sub> even after the loading of guest Ru nanoparticles. The S 2*p* spectra of In-O-MoS<sub>2</sub>@Ru and In-O-MoS<sub>2</sub> (Supplementary Fig. 8b) also demonstrate red-shifting tendency, in which the binding energies at 162.7 (S 2*p*<sub>1/2</sub>) and 161.5 (S 2*p*<sub>3/2</sub>) eV further confirm the existence of 1T MoS<sub>2</sub>. While for pure MoS<sub>2</sub>, the peaks at 163.2 and 162.0 eV are assigned to 2H phase<sup>16,21</sup>. Furthermore, in the In 3*d* spectrum of In-O-MoS<sub>2</sub>@Ru (Supplementary Fig. 8c), the peaks at 444.7 and 452.2 eV are attributed to In 3*d*<sub>5/2</sub> and In 3*d*<sub>3/2</sub>, implying that the doped indium atoms form metal-nonmetal bonding and demonstrate ionic characteristic<sup>31</sup>. As shown in the Ru 3*p* spectrum of In-O-MoS<sub>2</sub>@Ru (Supplementary Fig. 8d), the deconvoluted peaks centered at 461.1 and 483.5 eV are indexed to Ru<sup>0</sup> 3*p*<sub>3/2</sub> and Ru<sup>0</sup> 3*p*<sub>1/2</sub>. Meanwhile, the peaks at 463.3 and 485.5 eV are identified as Ru<sup>4+</sup> 3*p*<sub>3/2</sub> and Ru<sup>4+</sup> 3*p*<sub>1/2</sub><sup>32</sup>. This indicates that Ru nanoparticles in In-O-MoS<sub>2</sub>@Ru are governed by large proportion of metallic elements. Considering the slight negative shifting of Mo 3*d* binding energy of In-O-MoS<sub>2</sub>@Ru in comparison to that of In-O-MoS<sub>2</sub>, we infer that due to electronegativity differences between Ru element and matrix metal, electrons are inclined to transfer from metallic Ru to In-O-MoS<sub>2</sub>, resulting in the highly unoccupied Ru 4*d* orbitals. The optimized interfacial micro-environment induces electron delocalization around interface sites and thus enhances electronic coupling interaction between Ru nanoparticles with In-O-MoS<sub>2</sub>.

The X-ray absorption near-edge structure (XANES) and extended X-ray absorption fine structure (EXAFS) results provide further understanding towards the nature of coordination environment. In the In K-edge XANES spectrum in Fig. 3a, the absorption edge of In-O-MoS<sub>2</sub>@Ru is close to that of In<sub>2</sub>O<sub>3</sub> reference. According to the fitting analyzes by the first derivative of In K-edge XANES (Supplementary Fig. 9), the valence of In in In-O-MoS<sub>2</sub>@Ru is determined as 2.95. Specially, as seen in the In *k*<sup>3</sup>-weighted EXAFS spectrum in *R* space (Fig. 3b, nonphase-corrected), the dominant peak for the first shell corresponding to In-O scattering at 1.68 Å can be observed for In-O-MoS<sub>2</sub>@Ru with the absence of In-S and In-In signals<sup>33,34</sup>. Moreover, the weak peak at 2.88 Å is ascribed to In-M (In-Mo and In-Ru) scattering path in the second shell. According to the quantitative fitting results in Fig. 3c (*R* space), Supplementary Fig. 10 (*k* space) and Supplementary Table 1, the length of In-O bonding is 1.94 Å and each In atom is coordinated by ~6 neighboring O atoms, indicating the highly unsaturated coordination environment with superior catalytic activity. As shown in the Wavelet transform (WT) contour plot (Fig. 3d), In-O-MoS<sub>2</sub>@Ru demonstrates only one predominant intensity maximum at ~4.5 Å<sup>-1</sup> corresponding to In-O configuration, further confirming the atomically homogenous In-O dual-doping within MoS<sub>2</sub>. Herein, we infer that when great deals of In species are atomically incorporated within the MoS<sub>2</sub>, considerable oxygen atoms with high electronegativity inevitably take the place of partial sulfur atoms during hydrothermal synthesis process, which function as covalently bridging atoms to establish In-O rather than In-S bonding. It is quite different from those reported doped transition metal-S characteristics<sup>15,16,22,28,35</sup>. This suggests that In and O dual-doping reconstruct bulk MoS<sub>2</sub> lattices and thus offer the critical driving force for the formation of high-content 1T phase. In the In-O-MoS<sub>2</sub>@Ru catalyst, the extraneous In atoms can offer extra electrons to Mo *d* orbital and the incorporated O atoms can disturb the arrangement of neighboring S atoms. As a result, the simultaneous In-O co-dopants synergistically produce and further stabilize the metal phase MoS<sub>2</sub>. This result is consistent with the currently reported Co-O and Co-P co-doping triggered 1T phase MoS<sub>2</sub><sup>23,24</sup>.



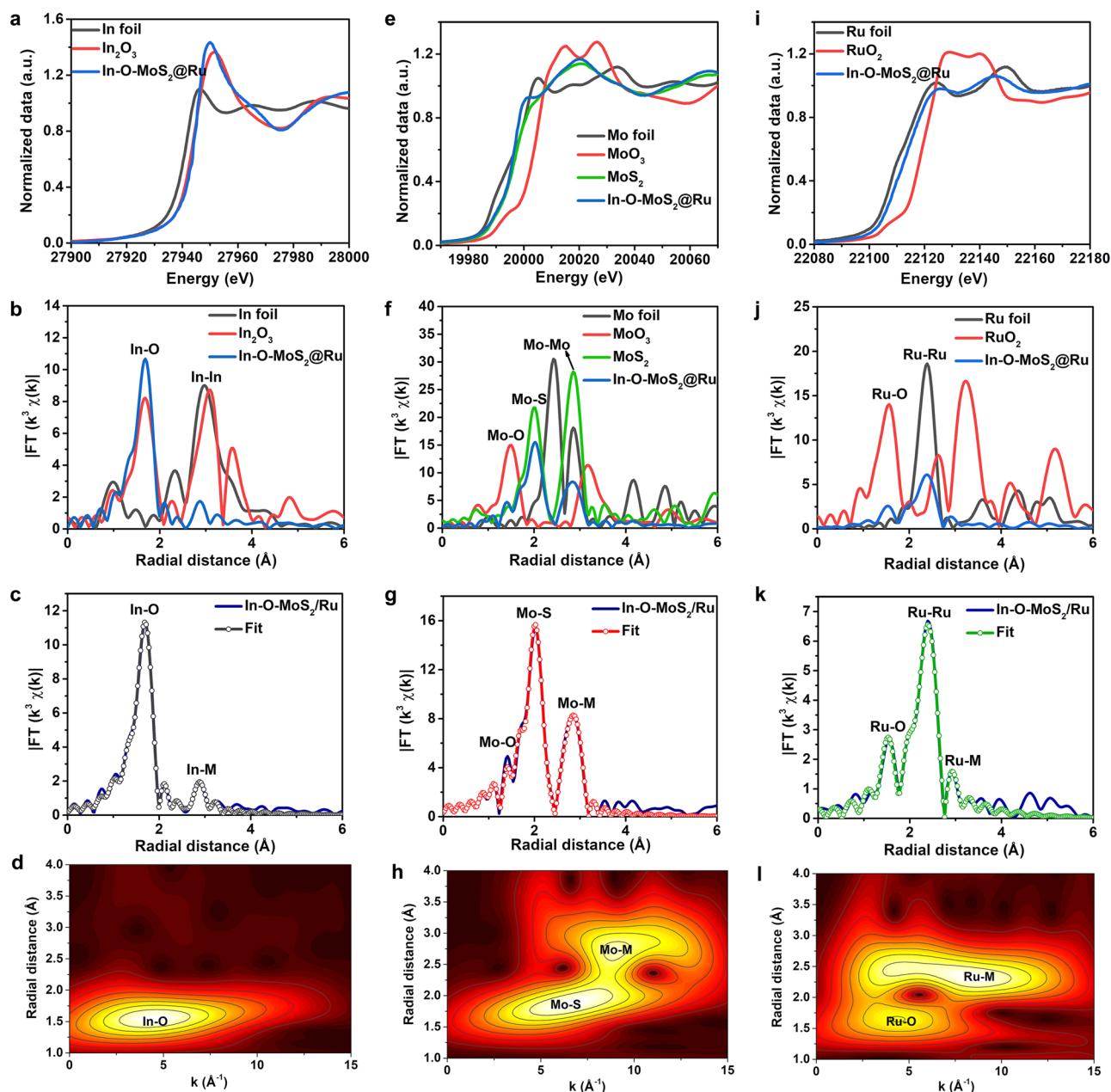


**Fig. 3 | X-ray absorption spectroscopy study of In-O-MoS<sub>2</sub>@Ru.** **a** Normalized In K-edge XANES spectra of In-O-MoS<sub>2</sub>@Ru, In<sub>2</sub>O<sub>3</sub> and In foil. **b** In K-edge k<sup>3</sup>-weighted EXAFS spectra at R-space of In-O-MoS<sub>2</sub>@Ru, In<sub>2</sub>O<sub>3</sub> and In foil. **c** In K-edge EXAFS fitting curves at R-space of In-O-MoS<sub>2</sub>@Ru. **d** Wavelet transforms for In K-edge EXAFS signals of In-O-MoS<sub>2</sub>@Ru. **e** Normalized Mo K-edge XANES spectra of In-O-MoS<sub>2</sub>@Ru, MoS<sub>2</sub>, MoO<sub>3</sub> and Mo foil. **f** Mo K-edge k<sup>3</sup>-weighted EXAFS spectra at R-space of In-O-MoS<sub>2</sub>@Ru, MoS<sub>2</sub>, MoO<sub>3</sub> and Mo foil. **g** Mo K-edge EXAFS fitting

curves at R-space of In-O-MoS<sub>2</sub>@Ru. **h** Wavelet transforms for Mo K-edge EXAFS signals of In-O-MoS<sub>2</sub>@Ru. **i** Normalized Ru K-edge XANES spectra of In-O-MoS<sub>2</sub>@Ru, RuO<sub>2</sub> and Ru foil. **j** Ru K-edge k<sup>3</sup>-weighted EXAFS spectra at R-space of In-O-MoS<sub>2</sub>@Ru, RuO<sub>2</sub> and Ru foil. **k** Ru K-edge EXAFS fitting curves at R-space of In-O-MoS<sub>2</sub>@Ru. **l** Wavelet transforms for Ru K-edge EXAFS signals of In-O-MoS<sub>2</sub>@Ru. Source data are provided as a Source Data file.

For the Mo K-edge XANES spectrum (Fig. 3e), the absorption edge position of In-O-MoS<sub>2</sub>@Ru is lower than that of pure MoS<sub>2</sub>, which is consistent with the XPS results in Supplementary Fig. 8a. As shown in the Mo EXAFS results in R space (Fig. 3f, nonphase-corrected), in contrast to pure MoS<sub>2</sub>, In-O-MoS<sub>2</sub>@Ru demonstrates much weaker intensity for Mo-Mo scattering peak, indicating the lower coordination number (CN). Together with the fitting parameters of In-O-MoS<sub>2</sub>@Ru (Fig. 3g; R space; Supplementary Fig. 11: k space) and MoS<sub>2</sub> (Supplementary Fig. 12: R space; Supplementary Fig. 13: k space), the Mo-Mo distance of In-O-MoS<sub>2</sub>@Ru (3.17 Å) is compressed compared to that of pure MoS<sub>2</sub> (3.6 Å). These results all further manifest the presence of 1 T

phase MoS<sub>2</sub> within the as-built In-O-MoS<sub>2</sub>@Ru catalyst<sup>24,36</sup>. Moreover, a small contribution of Mo-O can be fitted (CN=1.1) in the first shell, implying the successful of O doping within In-O-MoS<sub>2</sub>@Ru. The WT contour plot regarding Mo signals of In-O-MoS<sub>2</sub>@Ru in Fig. 3h also verifies the existence of Mo-nonmetal and Mo-metal paths. When coming to the Ru K-edge XANES results in Fig. 3i, for the In-O-MoS<sub>2</sub>@Ru catalyst, the valence state of the lattice-confined Ru nanoparticles is between those of Ru foil and RuO<sub>2</sub> species, and is much more close to that of Ru foil. This implies that metal Ru<sup>0</sup> is dominated in In-O-MoS<sub>2</sub>@Ru accompanied by a tiny proportion of oxidized Ru components, which is consistent with the XPS result in Supplementary

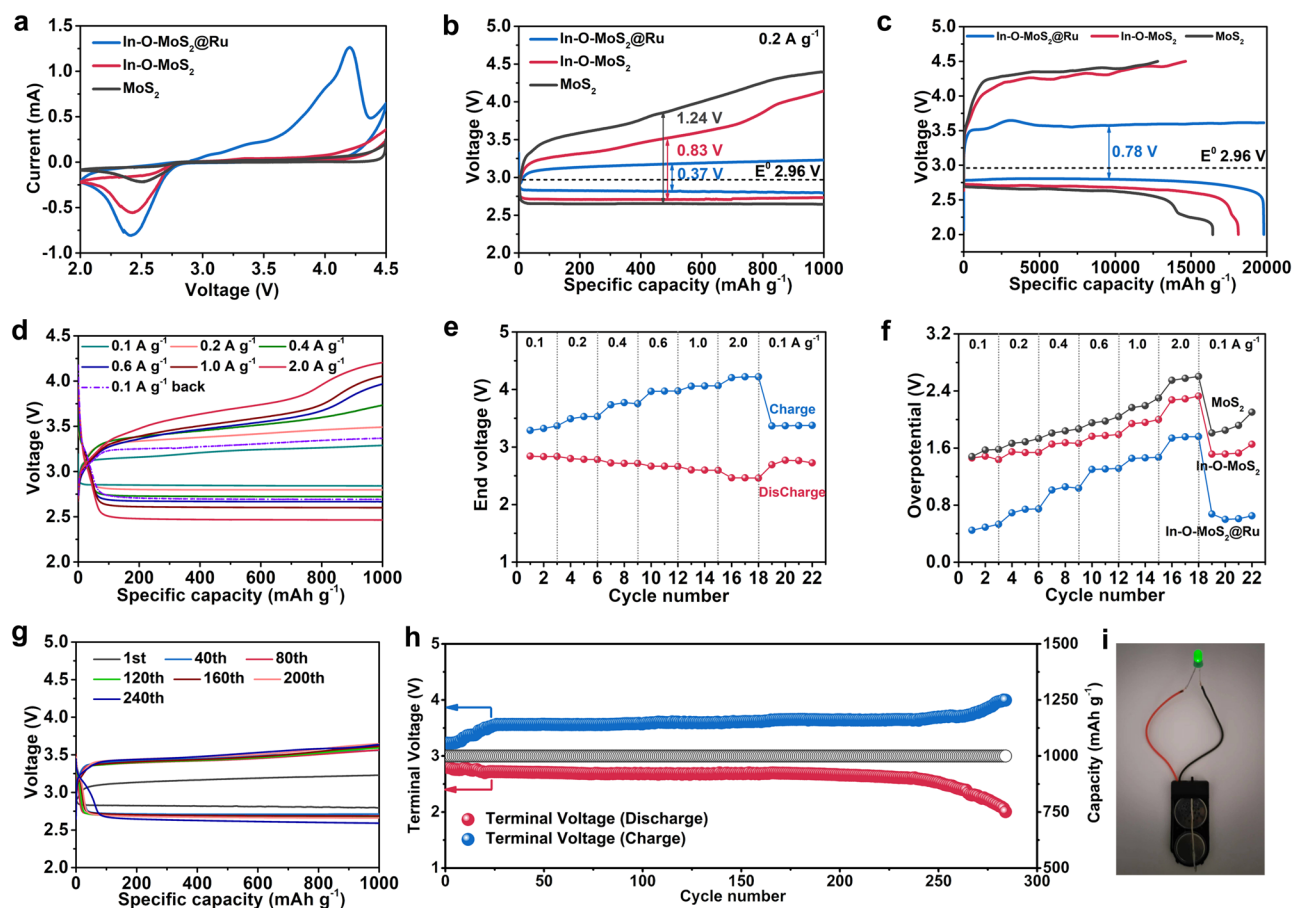


**Fig. 4 | Electrochemical performance of Li||O<sub>2</sub> batteries.** **a** CV profiles. **b** The discharge-charge curves under 200 mA g<sup>-1</sup> with a cut-off capacity of 1000 mAh g<sup>-1</sup>. **c** The deep discharge-charge curves between 2.0–4.5 V under 200 mA g<sup>-1</sup> of In-O-MoS<sub>2</sub>@Ru, In-O-MoS<sub>2</sub> and MoS<sub>2</sub>. Coulomb efficiency is the ratio of charge capacity to discharge capacity. **d** The rate performance at different specific currents for In-O-MoS<sub>2</sub>@Ru. **e** The end discharge/charge voltages at different specific currents for

In-O-MoS<sub>2</sub>@Ru. **f** The discharge/charge overpotentials at different specific currents for the three catalysts. **g** The discharge/charge profiles of In-O-MoS<sub>2</sub>@Ru at different cycles. **h** The cycling performance of In-O-MoS<sub>2</sub>@Ru at 200 mA g<sup>-1</sup> with a terminated capacity of 1000 mAh g<sup>-1</sup>. **i** Light up LED diode powered by In-O-MoS<sub>2</sub>@Ru based Li||air battery. Source data are provided as a Source Data file.

Fig. 8d. Furthermore, the fitted average oxidation number of Ru in In-O-MoS<sub>2</sub>@Ru is 0.82 (Supplementary Fig. 14). As evident from Figs. 3j–l, Supplementary Fig. 15 and Supplementary Table 1, In-O-MoS<sub>2</sub>@Ru demonstrates three scattering coordinations. The predominant peaks at 1.54 Å and 2.42 Å (in R space) are attributed to the Ru-O (*CN*=1.4) and Ru-Ru (*CN*=3.7) scattering paths in the first shell, respectively<sup>32,37</sup>. The peaks at 2.92 Å in R space is assigned to Ru-M (Ru-Mo and Ru-In) scattering path in the second shell. The emergence of Ru-M scattering feature is in accordance with that of In-M and Mo-M coordination environment in Figs. 3c and 3g, respectively. It further suggests that at the In-O-MoS<sub>2</sub>@Ru metal/support interface, the O doping within MoS<sub>2</sub> matrix plays a critical role in bridging with the epitaxially grown Ru nanoparticles. Furthermore, extra Ru-M coordination bonding manifests an efficient charge transfer between different metal centers, fully tailoring the charge state, local coordination environment as well as the electronic structure of catalytic sites. Specially, conventional heterogeneous interfaces are structurally non-coherent due to much large lattice misfit, which usually impose considerable barrier for charge transfer and suffer from phase separation during cycling<sup>38</sup>. In response, in this work, the well-designed lattice-grafting orientation relationship between Ru nanoparticles and In-O-MoS<sub>2</sub> substrate can trigger intense interfacial electronic coupling effect and establish solid metal-support interaction, beneficial for relieving charge diffusion limitation at hetero-interface, enhancing catalytic sites utilization efficiency and long-term stability.

### Electrochemical performance for Li||O<sub>2</sub> batteries

To verify our material strategy, In-O-MoS<sub>2</sub>@Ru, In-O-MoS<sub>2</sub> and MoS<sub>2</sub> as positive electrode catalysts are assembled into Li||O<sub>2</sub> coin cells. As shown in the cyclic voltammetry (CV) curves between 2.0 and 4.5 V in Fig. 4a, all the three catalysts demonstrate one dominant cathodic peak at about 2.44 V, corresponding to the generation of Li<sub>2</sub>O<sub>2</sub> during discharge ( $O_2 + 2Li^+ + 2e^- \rightarrow Li_2O_2$ ). Different from In-O-MoS<sub>2</sub> and MoS<sub>2</sub>, In-O-MoS<sub>2</sub>@Ru exhibits one additional anodic peak at 4.19 V during the Li<sub>2</sub>O<sub>2</sub> decomposition ( $Li_2O_2 \rightarrow O_2 + 2Li^+ + 2e^-$ ), implying its different OER reaction pathway<sup>39,40</sup>. Moreover, both the reduction/oxidation peak currents and integration regions of In-O-MoS<sub>2</sub>@Ru are much higher than those of In-O-MoS<sub>2</sub> and MoS<sub>2</sub>. It suggests that more Li<sub>2</sub>O<sub>2</sub> species can be produced with In-O-MoS<sub>2</sub>@Ru catalyst during discharge process, bringing out a much higher discharge capacity. And the as-achieved Li<sub>2</sub>O<sub>2</sub> can also be fully decomposed during the following recharge process, indicating a much better ORR/OER reversibility. Furthermore, In-O-MoS<sub>2</sub>@Ru possesses a much lower OER onset potential, which further discloses the decomposition of the involved Li<sub>2</sub>O<sub>2</sub> species overwhelms lower energy barrier, rendering its enhanced OER kinetics and better energy efficiency. As shown in Fig. 4b, when tested under 200 mA g<sup>-1</sup> with a cut-off capacity of 1000 mA h g<sup>-1</sup>, the positive electrode catalyzed by In-O-MoS<sub>2</sub>@Ru features an ameliorated discharge/charge polarization of 0.37 V with a higher round-trip efficiency of 88.5%. By contrast, the discharge/charge overpotentials of In-O-MoS<sub>2</sub> and MoS<sub>2</sub> are 0.83 and 1.24 V, with reduced round-trip

efficiencies of 76.7% and 68.2%, respectively. Figure 4c are the deep galvanostatic discharge-charge profiles during the first cycle between 2.0–4.5 V under 200 mA g<sup>-1</sup>. During discharge, In-O-MoS<sub>2</sub>@Ru maintains a considerably wide discharge capacity interval under a steady discharge voltage close to 2.79 V, during which Li<sub>2</sub>O<sub>2</sub> can homogeneously nucleate and constantly deposit on the In-O-MoS<sub>2</sub>@Ru catalyst surface. During the subsequent recharge, for In-O-MoS<sub>2</sub>@Ru, the charge voltage first creeps up to 3.5 V, which is associated with the preferential decomposition of Li<sub>2</sub>O<sub>2</sub> close to the catalyst's surface. Then the charge voltage is slightly fluctuated within a large capacity interval, corresponding to the continuous oxidization of residual Li<sub>2</sub>O<sub>2</sub>. It suggests that the Li<sub>2</sub>O<sub>2</sub> products on the In-O-MoS<sub>2</sub>@Ru surface can feasibly decompose under a much lower voltage range, inducing an extremely small charge polarization of only 0.78 V. In sharp contrast, the charge potential of the MoS<sub>2</sub> positive electrode rapidly increases to 4.25 V, indicating that the following Li<sub>2</sub>O<sub>2</sub> decomposition proceeds at a much higher voltage level accompanied by larger energy consumption. This finally leads to a severe charge polarization of up to 1.40 V for MoS<sub>2</sub>. As a result, In-O-MoS<sub>2</sub>@Ru delivers much higher discharge/charge capacity of 19800 mAh g<sup>-1</sup> accompanied by a Coulombic efficiency (CE) value of 100.0%. However, the discharge/charge capacities of In-O-MoS<sub>2</sub> and MoS<sub>2</sub> are 18119/14642 mAh g<sup>-1</sup> and 16433/12805 mAh g<sup>-1</sup> with CE values of 80.8% and 77.9%, respectively. The simultaneous improvement of discharge/charge capacity and energy efficiency underscores the positive effects of In-O co-doping and lattice-grafted Ru nanoparticles on the catalytic kinetics of In-O-MoS<sub>2</sub>@Ru.

The rate performances of the three catalysts are evaluated under various specific currents from 0.1 to 2.0 A g<sup>-1</sup> with a fixed capacity of 1000 mA h g<sup>-1</sup>. As shown in Fig. 4d and Supplementary Fig. 16, compared to In-O-MoS<sub>2</sub> and MoS<sub>2</sub>, the In-O-MoS<sub>2</sub>@Ru positive electrode demonstrates flatter discharge/charge plateaus and much-alleviated overvoltage under both small and large specific currents. For instance, despite at 2.0 A g<sup>-1</sup>, the ending discharge and charge voltages can still be maintained at 2.47 and 4.21 V with an overpotential of only 1.74 V, far below that of In-O-MoS<sub>2</sub> (2.28 V) and MoS<sub>2</sub> (2.55 V). Figure 4e and Supplementary Fig. 17 are the corresponding discharge/charge ending voltages of In-O-MoS<sub>2</sub>@Ru, In-O-MoS<sub>2</sub> and MoS<sub>2</sub> when continuously cycling at different applied specific currents and Fig. 4f demonstrates the summary overpotential results. Undoubtedly, the terminated charge voltages of In-O-MoS<sub>2</sub>@Ru stayed below 4.23 V even at large specific currents. However, for In-O-MoS<sub>2</sub> and MoS<sub>2</sub>, the ending charge voltages exceeded 4.5 V under 1.0 A g<sup>-1</sup>. As a result, when cycled at 1.0 A g<sup>-1</sup> and 2.0 A g<sup>-1</sup>, the voltage gaps of In-O-MoS<sub>2</sub>@Ru are located at 1.45–1.47 V and 1.74–1.76 V, respectively, which are much lower than that of In-O-MoS<sub>2</sub> (1.94–2.00 V and 2.27–2.33 V) and MoS<sub>2</sub> (2.16–2.30 V and 2.55–2.60 V). When the specific current recovers to 0.1 A g<sup>-1</sup>, the overpotential of In-O-MoS<sub>2</sub>@Ru is maintained at a low value of 0.60 V, demonstrating better rate stability. While for In-O-MoS<sub>2</sub> and MoS<sub>2</sub>, the overpotentials reach up to 1.65 and 2.10 V. Furthermore, the cycling stability of In-O-MoS<sub>2</sub>@Ru at 200 mA g<sup>-1</sup> with a curtailed capacity of 1000 mA h g<sup>-1</sup> are demonstrated in Fig. 4g, h. In-O-MoS<sub>2</sub>@Ru delivers a better cycle life up to 284 cycles, surpassing that of In-O-MoS<sub>2</sub> (122 cycles, Supplementary Fig. 18a, c) and MoS<sub>2</sub> (83 cycles, Supplementary Fig. 18b, c). More importantly, the cut-off discharge and charge voltages of In-O-MoS<sub>2</sub>@Ru can be readily controlled >2.5 V and <3.7 V without wild fluctuation before the 250<sup>th</sup> cycle, which play a critical role in restraining electrolyte decomposition and the derived parasitic products. Furthermore, as shown in Supplementary Fig. 19a, b, the In-O-MoS<sub>2</sub>@Ru positive electrode can steady run for 29 cycles (870 h) even at a much larger cut-off capacity of 6000 mA h g<sup>-1</sup> at a specific current of 400 mA g<sup>-1</sup>. The much-enhanced high rate capability and prolonged cycling span of In-O-MoS<sub>2</sub>@Ru are originated from the synergistic mechanisms by In-O heterogeneous atom doping and the strong hetero-interface

interaction between the grafted Ru nanoparticles and In-O-MoS<sub>2</sub>, which facilitate the repeated O<sub>2</sub> reduction/evolution in Li||O<sub>2</sub> batteries. The as-desired electronic structure modulation between multi-type metallic sites makes great contributions to the ORR/OER bifunctional catalytic activity of In-O-MoS<sub>2</sub>@Ru. More importantly, as shown in Supplementary Fig. 20, the In-O-MoS<sub>2</sub>@Ru equipped Li||air battery can still readily run for 98 cycles (392 h) at actual air atmosphere, far exceeding that of MoS<sub>2</sub> (20 cycles, 80 h), further demonstrating the much ameliorated dual-functional catalytic kinetics and long-term cycle life for In-O-MoS<sub>2</sub>@Ru. This grants In-O-MoS<sub>2</sub>@Ru good application prospects towards real lithium-air batteries. As shown in Fig. 4i, a LED diode with green color can be successfully lighted up by the In-O-MoS<sub>2</sub>@Ru equipped lithium||air batteries.

### Ex situ analysis after discharge and charge

To gain deeper insights into the redox mechanism, a series of ex-situ microstructure characterizations on Li<sub>2</sub>O<sub>2</sub> species after discharge/charge state are performed. The post-cycling XRD patterns in Fig. 5a suggest that after discharge, all the three positive electrodes demonstrate a diffraction peak at 35.1° assigned to the (101) planes of Li<sub>2</sub>O<sub>2</sub>, which completely disappears after recharge process<sup>41,42</sup>. It suggests that the discharge/charge capacities are dominated by the contribution from the reversible formation and decomposition of Li<sub>2</sub>O<sub>2</sub> species. However, the Li<sub>2</sub>O<sub>2</sub> characteristic peak intensity for In-O-MoS<sub>2</sub>@Ru is much weaker in comparison with that of In-O-MoS<sub>2</sub> and MoS<sub>2</sub>, suggesting the weak crystallinity of the as-formed Li<sub>2</sub>O<sub>2</sub> after discharge. In general, the integral area of Li<sub>2</sub>O<sub>2</sub> peak is proportional to the capacity contribution from the crystalline state of Li<sub>2</sub>O<sub>2</sub>. While the discharge capacity is the combination of crystalline and amorphous Li<sub>2</sub>O<sub>2</sub>, which cannot be recognized by XRD characterization<sup>43</sup>. CV data shows that In-O-MoS<sub>2</sub>@Ru possess a much larger capacity, thus, it suggests a large amount of the Li<sub>2</sub>O<sub>2</sub> species are amorphous during the discharge-process, which are favorable for decomposition during subsequent recharge. The discharged In-O-MoS<sub>2</sub>@Ru still presents the self-assembly nanosheets morphology (Supplementary Figs. 21a, b), indicating that an amorphous Li<sub>2</sub>O<sub>2</sub> thin films is homogeneously covered on the In-O-MoS<sub>2</sub>@Ru surface. HRTEM images in Fig. 5b, c further illustrate the continuous Li<sub>2</sub>O<sub>2</sub> thin layers with an average thickness of 5 nm are compactly grown over the whole In-O-MoS<sub>2</sub>@Ru nanosheets. In particular, no distinct lattice fringe can be observed across the Li<sub>2</sub>O<sub>2</sub> domains, verifying its amorphous characteristic. Aided by electron energy loss spectroscopy (EELS) spectra (Fig. 5d, e), the distinct Li K and O K-edges signals can be simultaneously collected around the In-O-MoS<sub>2</sub>@Ru surface, confirming the surface coating layer is Li<sub>2</sub>O<sub>2</sub><sup>44,45</sup>. In sharp contrast, as shown in Supplementary Fig. 21c, after discharge, great deals of Li<sub>2</sub>O<sub>2</sub> nanosheets with thickness of about 20 nm are deposited on the surface area of In-O-MoS<sub>2</sub>, inducing the active sites passivation. What is worse, as shown in Supplementary Fig. 21d for pure MoS<sub>2</sub>, large-sized bulk Li<sub>2</sub>O<sub>2</sub> aggregates block the efficient tri-phase active regions, which severely impede the mass and charge diffusion channels. This poses tough obstacle for the high-efficiency decomposition of discharge products during recharge. Evidenced by the above-mentioned proofs, the In-O dual doping can effectively refrain from the Li<sub>2</sub>O<sub>2</sub> nanosheet agglomeration. And due to the coordination effect from the In-O dual doping and lattice-grafted Ru nanoparticles, the morphology and crystalline characteristic of Li<sub>2</sub>O<sub>2</sub> as well as the discharge product/catalyst interface are fundamentally optimized. The performance advantages of a thin Li<sub>2</sub>O<sub>2</sub> layer can be summarized in two points: a) The ionic conductivity of the amorphous Li<sub>2</sub>O<sub>2</sub> is 12 times larger than that of crystalline phase<sup>46,47</sup>. Together with the nano-scale thickness of Li<sub>2</sub>O<sub>2</sub> and the high surface area of the substrate, the transfer impedances of Li<sup>+</sup>, e<sup>-</sup> and O<sub>2</sub> across the Li<sub>2</sub>O<sub>2</sub>/catalyst interface are reduced; b) Due to compact interfacial contact between the Li<sub>2</sub>O<sub>2</sub> and In-O-MoS<sub>2</sub>@Ru matrix, the catalysis efficiency of In-O-MoS<sub>2</sub>@Ru can be maximized, further accelerating the



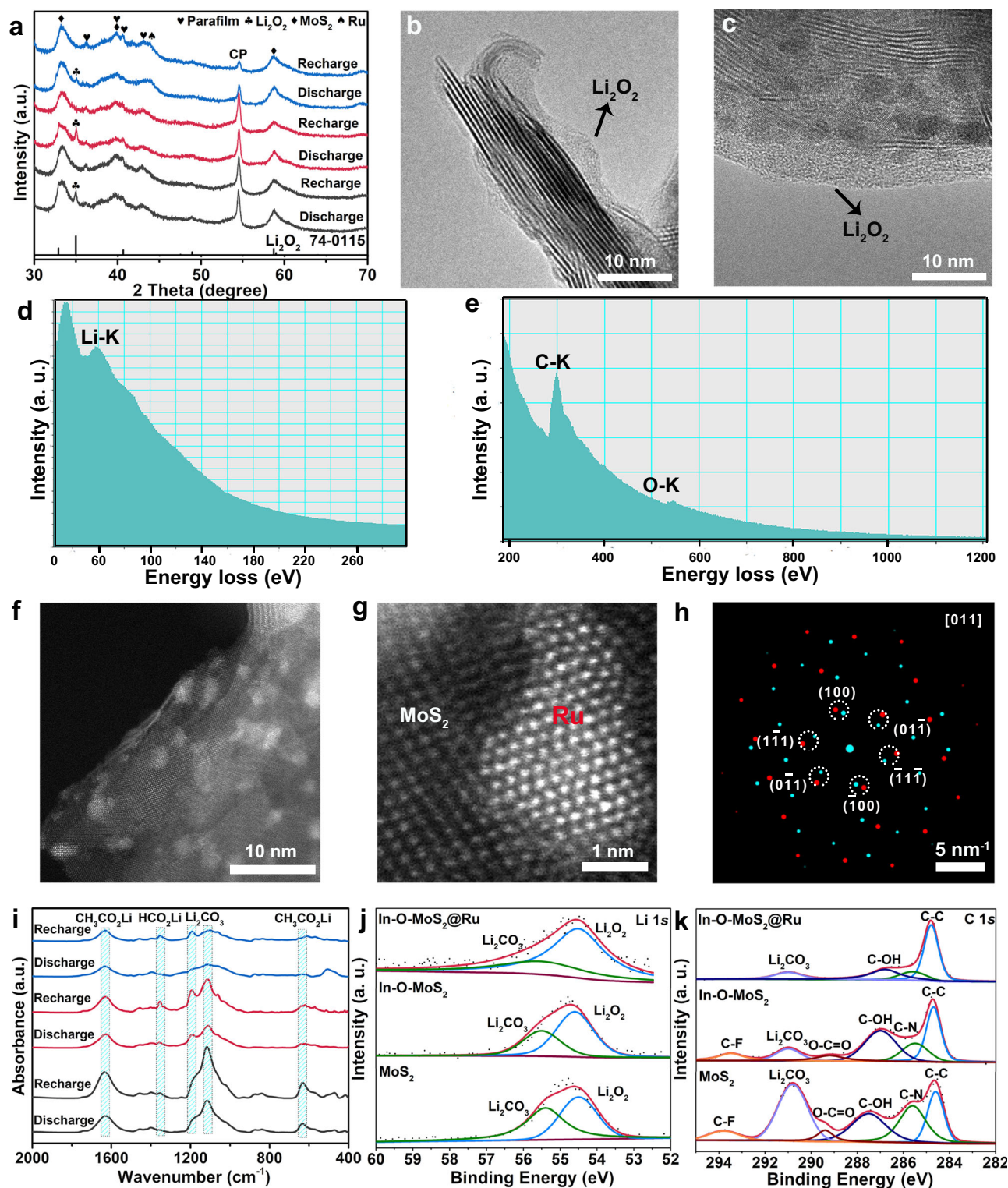


**Fig. 5 | Ex situ analysis after discharge and charge.** **a** Ex situ XRD patterns of the discharged/charged In-O- $\text{MoS}_2$ @Ru, In-O- $\text{MoS}_2$  and  $\text{MoS}_2$  electrodes during the first cycle between 2.0–4.5 V at 200  $\text{mA g}^{-1}$ . The Paraform was used for protecting the electrode slices from the air. Ex situ bright-field TEM images (**b–c**), EELS profile of Li-K edge (**d**), EELS profile of O-K edge (**e**) of In-O- $\text{MoS}_2$ @Ru after discharge to 2.0 V at 200  $\text{mA g}^{-1}$ . Ex situ high-angle annular dark-field STEM images (**f, g**), simulated SAED patterns (**h**) of In-O- $\text{MoS}_2$ @Ru after 284 cycles with a cut-off

capacity of 1000  $\text{mAh g}^{-1}$  at 200  $\text{mA g}^{-1}$ . **i** EX situ FTIR spectra of the discharged/charged In-O- $\text{MoS}_2$ @Ru (blue profiles), In-O- $\text{MoS}_2$  (red profiles) and  $\text{MoS}_2$  (black profiles) electrodes during the 60<sup>th</sup> cycle with a cut-off capacity of 1000  $\text{mAh g}^{-1}$  at 200  $\text{mA g}^{-1}$ . Ex situ XPS spectra of the In-O- $\text{MoS}_2$ @Ru, In-O- $\text{MoS}_2$  and  $\text{MoS}_2$  electrodes in Li 1s (**j**) and C 1s (**k**) regions after the 60<sup>th</sup> cycle with a cut-off capacity of 1000  $\text{mAh g}^{-1}$  at 200  $\text{mA g}^{-1}$ . Source data are provided as a Source Data file.

reversible decomposition kinetics. This is consistent with the reduced charge transfer resistance observed in the electrochemical impedance spectroscopy results for the In-O-MoS<sub>2</sub>@Ru electrode (Supplementary Fig. 22). Correspondingly, these account for the intrinsic reasons of the exceptional OER catalytic activity of In-O-MoS<sub>2</sub>@Ru.

Crucially, to verify the catalyst stability after long-period cycling, the HAADF-STEM images and simulated SAED patterns of In-O-MoS<sub>2</sub>@Ru after 284 cycles are demonstrated in Fig. 5f–h. The active catalyst is preserved as In-O-MoS<sub>2</sub>@Ru with the absence of obvious reconstruction or structural collapse. Importantly, In-O-MoS<sub>2</sub>@Ru demonstrates good tolerance to agglomeration while maintaining lattice grafting structure. In conclusion, these results clearly suggest that thanks to the In-O doping induced stabilization effect on 1T MoS<sub>2</sub> matrix and lattice epitaxy boosted stabilization promotion on hetero-interface, the as-constructed In-O-MoS<sub>2</sub>@Ru hybrid is indeed a robust catalyst for Li||O<sub>2</sub> batteries. Furthermore, Fourier transformed infrared (FTIR) spectra (Fig. 5f) are implemented to study the accumulated parasitic products after long-period cycling. Despite running for 60 consecutive cycles, the cycled In-O-MoS<sub>2</sub>@Ru electrode demonstrates weaker side product signals. In sharp contrast, distinct side products characteristic peaks embracing Li<sub>2</sub>CO<sub>3</sub> (1192, 1456 cm<sup>-1</sup>), HCOOLi (1354 cm<sup>-1</sup>) and CH<sub>3</sub>COOLi (624, 1627 cm<sup>-1</sup>) are inevitably detected from the cycled In-O-MoS<sub>2</sub> and MoS<sub>2</sub> positive electrodes, which are the potential culprit for the catalytic sites poisoning and battery failure<sup>48,49</sup>. According to the ex situ Li 1s (Fig. 5j) and C 1s (Fig. 5k) XPS results of the 60<sup>th</sup> cycle, the major proportion of Li<sub>2</sub>O<sub>2</sub> and minor side products can be observed for the In-O-MoS<sub>2</sub>@Ru electrode<sup>50</sup>. It is concluded that due to the enhanced catalytic efficiency and reduced charging overpotential, In-O-MoS<sub>2</sub>@Ru possesses better long-periodic tolerance to the generation and accumulation of parasitic products.

### DFT calculations and proposed mechanisms

Density functional theory (DFT) calculations are further employed to investigate the essential reason for the improved performance in Li||O<sub>2</sub> batteries. Source data are provided as a Supplementary Data 1 file. The optimized geometries of 2H-MoS<sub>2</sub>, 1T-MoS<sub>2</sub>, In-O-MoS<sub>2</sub>, and In-O-MoS<sub>2</sub>@Ru are displayed in Supplementary Fig. 23, respectively. As shown in the side view of the unoccupied orbital close to Fermi level of In-O-MoS<sub>2</sub> (the lower plane) and 1T-MoS<sub>2</sub> (the upper plane) in Fig. 6a, the number of unoccupied orbitals perpendicular to the basal plane is reduced in In-O-MoS<sub>2</sub>. Moreover, the electron density difference analysis of In-O-MoS<sub>2</sub> and 1T-MoS<sub>2</sub> (the lower and upper plane) in Fig. 6b shows that after the involvement of In-O co-doping, the S element undergoes further sp<sup>3</sup> inequality hybridization, where the contribution of sp<sup>3</sup> orbitals to the vertical direction is reduced, while the orbital contribution to the direction of Mo and S bond is increased. This implies that the chemical bonding is strengthened and thus contributes to the intrinsic stability of In-O-MoS<sub>2</sub> than that of 1T MoS<sub>2</sub>. The density of states (DOS) analysis (Fig. 6c, Supplementary Fig. 24) manifest that the valence electron energy band near Fermi level of Mo is shifted up from -3.53 to -3.24 for occupied states and from 1.33 to 1.94 for unoccupied states in MoS<sub>2</sub> and In-O-MoS<sub>2</sub>, respectively. While the occupied and unoccupied valence band center of interface S are shifted up from -3.80 to -3.41 and from 1.24 to 1.90, respectively, implying the number of occupied antibonding states is reduced and the bonding strength is enhanced. These factors contribute to the much-improved inherent stability of the 1T phase structure in In-O-MoS<sub>2</sub>. Furthermore, as shown in the electron density difference slice (Fig. 6d) and the electrostatic potential mapping (Supplementary Fig. 25) of In-O-MoS<sub>2</sub>@Ru, after lattice confining of Ru nanoparticle, there constructs a stable interface-contact between Ru and In-O-MoS<sub>2</sub>, where Ru nanoparticle plays a role in electron-injection, and the electrons tend to transfer from Ru nanoparticle with a higher electron potential to the In-O-MoS<sub>2</sub> substrate. The energy bands (Supplementary Fig. 26) of

both the Ru nanoparticle and In-O-MoS<sub>2</sub> are widened, also supporting the stronger electron interaction within In-O-MoS<sub>2</sub>@Ru. From the orbital analysis of Fig. 6e, it can be seen that the orbitals have good delocalization in the system of In-O-MoS<sub>2</sub>@Ru and the orbitals from Ru and Mo have contributions to the unoccupied orbitals near Fermi-level. Since the orbital distribution of Mo are in the central sublayer with unfavorable steric effect, the active orbitals near Fermi-level accepting electron transfer mainly come from the Ru constituent in In-O-MoS<sub>2</sub>@Ru. This implies that the lattice grafted Ru nanoparticle is the most favorite active site to accept electrons from the electrode and transfer it to the adsorbed catalytic species on the interface, devoting to the enhanced-reactivity of In-O-MoS<sub>2</sub>@Ru.

Since the electrochemical reaction in Li||O<sub>2</sub> battery includes the activation of oxygen and migration of Li ion to form Li<sub>2</sub>O<sub>2</sub> during ORR, the O<sub>2</sub> activation capability and the binding energy difference between LiO<sub>2</sub> and Li<sub>2</sub>O<sub>2</sub> on the electrode are calculated to evaluate the electrode reaction dynamics. As shown in Fig. 6f, the In-O-MoS<sub>2</sub>@Ru interface is more preferable for the activation of the O<sub>2</sub> molecule with a larger binding energy (-6.9 eV) and the complete cleavage of O-O bond even without the electron injection from the electrode. In contrast, MoS<sub>2</sub> and In-O-MoS<sub>2</sub> have weaker adsorption energy (-0.12 eV, -0.17 eV). As shown in Fig. 6g, the adsorption of LiO<sub>2</sub> and Li<sub>2</sub>O<sub>2</sub> on In-O-MoS<sub>2</sub>@Ru has smaller binding energy difference (0.13 eV) than those of In-O-MoS<sub>2</sub> (0.18 eV) and MoS<sub>2</sub> (0.44 eV), suggesting the In-O-MoS<sub>2</sub>@Ru catalyst has the more favorable Li ion migration efficiency to form the Li<sub>2</sub>O<sub>2</sub> species or release back to isolated state between both electrodes. This is consistent with the much lower experimental over-potential observed for In-O-MoS<sub>2</sub>@Ru (Fig. 4b, c). Hence, there should be different reaction mechanisms on the three kinds of catalysts. For MoS<sub>2</sub> and In-O-MoS<sub>2</sub>, the Li<sup>+</sup> is closer to the interface than active O<sub>2</sub>, and the O-O bond is slightly elongated relative to that in adsorbed O<sub>2</sub>. This implies that the oxygen has very weak activation tendency on the surface of MoS<sub>2</sub> and In-O-MoS<sub>2</sub> even with the involvement of electrons and Li<sup>+</sup>. On the other hand, the In-O-MoS<sub>2</sub>@Ru could efficiently activate the O<sub>2</sub> molecule directly ahead of the electron transfer. According to the experimental and calculation results, the possible reaction mechanism and the morphological evolution of the discharge products during the ORR process are proposed. At the beginning, O<sub>2</sub> obtains an electron from the electrode to produce LiO<sub>2</sub> intermediate through a one-electron reduction reaction (O<sub>2</sub> + e<sup>-</sup> + Li<sup>+</sup> → LiO<sub>2</sub>). For In-O-MoS<sub>2</sub>@Ru, first, due to In-O doping stabilized 1T phase MoS<sub>2</sub>, fast electron conduction through the whole matrix is promoted. Second, due to the much enhanced O<sub>2</sub> affinity and O-O bond breakage capability stemming from In-O doping modulated Ru nanoparticle, O<sub>2</sub> can quickly diffuses to the catalyst surfaces and be reduced to LiO<sub>2</sub>. Therefore, a large number of evenly distributed nucleation centers are constructed, numerous LiO<sub>2</sub> nuclei can be quickly generated along the entire matrix of In-O-MoS<sub>2</sub>@Ru. Then due to the intense interaction between In-O-MoS<sub>2</sub>@Ru and LiO<sub>2</sub>, the confined LiO<sub>2</sub> can be further quickly converted to Li<sub>2</sub>O<sub>2</sub> via a surface electrochemical reduction reaction (LiO<sub>2</sub> + Li<sup>+</sup> + e<sup>-</sup> → Li<sub>2</sub>O<sub>2</sub>). At this stage, the growth of Li<sub>2</sub>O<sub>2</sub> along the thickness direction is largely limited during the successive ORR process, contributing to the formation of abundant poorly crystallized Li<sub>2</sub>O<sub>2</sub> thin layers closely covered on the In-O-MoS<sub>2</sub>@Ru surface. This contributes to good decomposition efficiency and thus low ORR/OER overpotential. For In-O-MoS<sub>2</sub>, although the charge transfer is enhanced, due to the lower binding energy towards oxygen containing reactants, the part of the LiO<sub>2</sub> may dissolve in electrolyte and transform into the large-sized flake-like Li<sub>2</sub>O<sub>2</sub> via a solution-mediated pathway (2LiO<sub>2</sub> → Li<sub>2</sub>O<sub>2</sub> + O<sub>2</sub>). While for pure MoS<sub>2</sub>, the inferior electron conductivity and limited adsorption site for LiO<sub>2</sub> finally cause large Li<sub>2</sub>O<sub>2</sub> aggregates deposit on the MoS<sub>2</sub> surface. These discharge products are difficult to be decomposed and thus induce severe OER polarization. Therefore, the favorable oxygen activation ability and the relaxed migration of Li ion



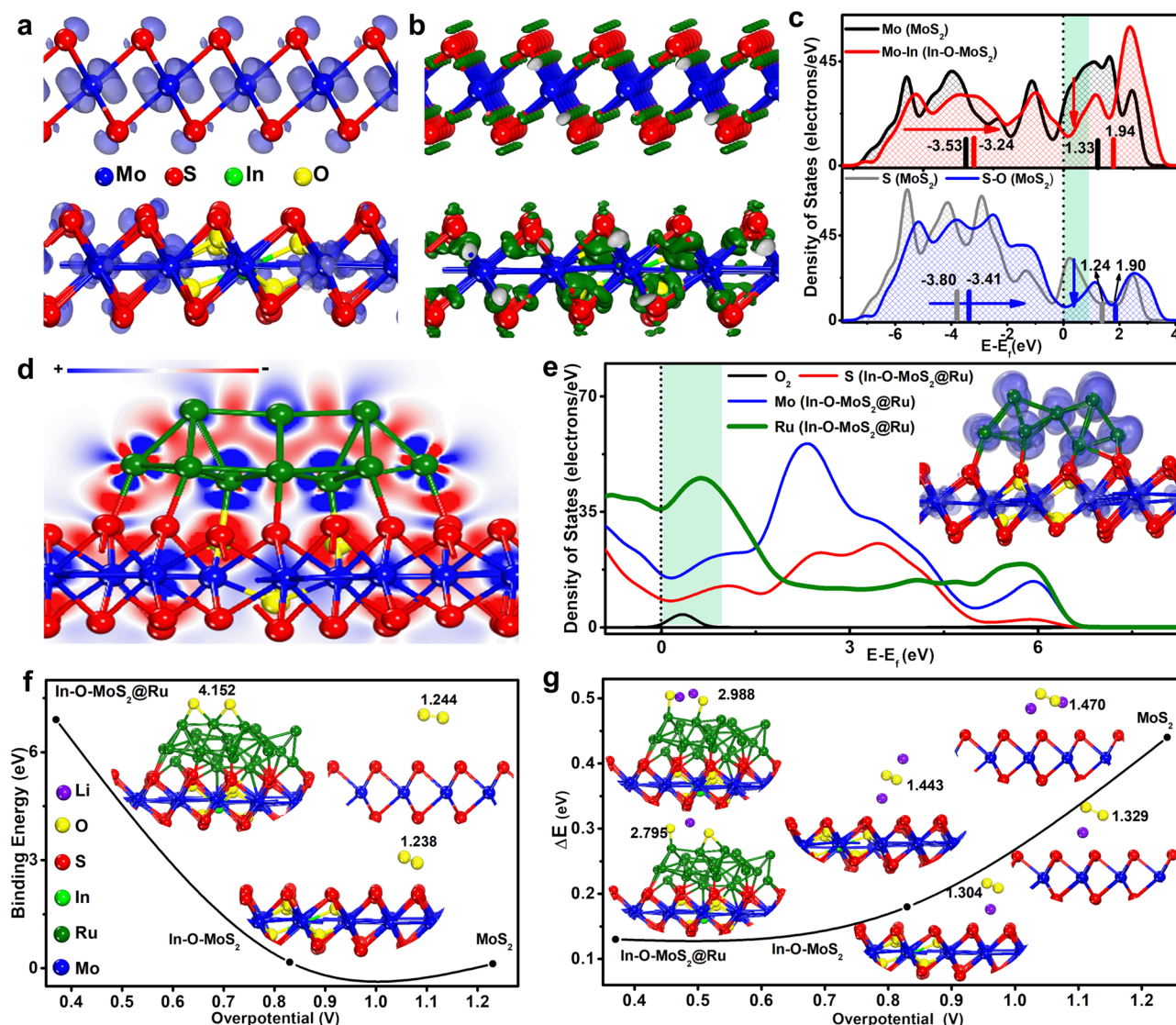


**Fig. 6 | DFT calculations.** The Mo, Ru, In, S, O, and Li atoms are described by blue, dark green, green, red, yellow and purple balls, respectively. **a** The side views of the unoccupied orbital near Fermi level of 1T-MoS<sub>2</sub> (top) and In-O-MoS<sub>2</sub> (down). **b** The side views of the electron density difference of 1T-MoS<sub>2</sub> (top) and In-O-MoS<sub>2</sub> (down). **c** The PDOS of Mo&Mo-In and S&S-O in MoS<sub>2</sub> and In-O-MoS<sub>2</sub>. **d** The side-view electron density difference slice of In-O-MoS<sub>2</sub>@Ru. **e** The DOS plots with the

visualized unoccupied orbital mapping of In-O-MoS<sub>2</sub>@Ru. **f** The relative energy diagram with structural information for the O<sub>2</sub> adsorption on MoS<sub>2</sub>, In-O-MoS<sub>2</sub> and In-O-MoS<sub>2</sub>@Ru. **g** The relative energy difference with structural information between the LiO<sub>2</sub> and Li<sub>2</sub>O<sub>2</sub> adsorption on MoS<sub>2</sub>, In-O-MoS<sub>2</sub> and In-O-MoS<sub>2</sub>@Ru. Source data are provided as a Source Data file.

at In-O-MoS<sub>2</sub>@Ru interface guarantee the preferable reaction dynamics and the optimum Li||O<sub>2</sub> battery performance.

## Discussion

In conclusion, 1T MoS<sub>2</sub> supported metal nanoparticle catalysts are highly appealing but face the fundamental challenge of thermal metastability. Here, we reveal a fresh atomic p-block In-O stabilized 1T MoS<sub>2</sub> with epitaxially connected Ru nanocrystals enabling bifunctional catalysis activity and stability for Li||O<sub>2</sub> batteries. Experimental results and DFT calculations disclose the special atomic-level In-O doping has assumed two decisive roles in the present work. First, In doping induces stronger *s/p* electron coupling interaction within MoS<sub>2</sub>, which results in the lower bonding orbital and higher antibonding orbital. While partially substituting S with O further facilitates intensifying the nonequivalent sp<sup>3</sup> hybridization. That reduces the interface vertical orbital orientation and increases the inherent electronic coupling, contributing to stabilizing high-content 1T phase MoS<sub>2</sub>. Second, by in situ introduced In-O mediation, the guest Ru nanoparticles can be

epitaxially grown from the lattice of In-O-MoS<sub>2</sub> matrix, establishing robust lattice-grafting hetero-interface. The cooperative In-O-MoS<sub>2</sub>@Ru catalyst with optimized electronic structure can greatly facilitate enhancing O<sub>2</sub> activation capability and charge transfer efficiency. This contributes to inducing the formation of amorphous ultra-thin Li<sub>2</sub>O<sub>2</sub> films during ORR, which are more readily decomposed during OER, efficiently decreasing redox barriers and enhancing bifunctional catalytic kinetics. We believe this work paves a avenue of constructing high-efficiency electrocatalysts by synergizing phase engineering and lattice coherency strategy for metal||air batteries.

## Methods

### Catalyst synthesis

**Preparation of In-O-MoS<sub>2</sub>, In-MoS<sub>2</sub>, MoS<sub>2</sub>.** First, 0.34 g ammonium heptamolybdate ((NH<sub>4</sub>)<sub>6</sub>Mo<sub>7</sub>O<sub>24</sub>·4H<sub>2</sub>O, Sinopharm Chemical Reagent Co., Ltd., ≥ 99.0%) and 1.39 g thiourea (Sinopharm Chemical Reagent Co., Ltd., ≥ 99.0%) was uniformly dissolved in into 50 mL deionized water. Afterwards, 0.019 g indium(III) chloride tetrahydrate



( $\text{InCl}_3 \cdot 4\text{H}_2\text{O}$ , Sinopharm Chemical Reagent Co., Ltd.,  $\geq 99.0\%$ ) was slowly added into the transparent solution, then 2.5 mL concentrated hydrochloric acid (Sinopharm Chemical Reagent Co., Ltd., 36.0–38.0%) was added to adjust the pH value close to 1. After magnetic stirring for 0.5 h, the mixed solution was pour into Teflon-lined autoclave (100 mL) and experienced the hydrotherm treatment at 200 °C for 24 h. Then the black sediment was collected by repeated centrifugation at 8000  $\text{r min}^{-1}$  and alternately washed with deionized water and ethyl alcohol (Sinopharm Chemical Reagent Co., Ltd.,  $\geq 99.5\%$ ) for six times. After vacuum-drying at 60 °C for 12 h, In-O-MoS<sub>2</sub> powders could be achieved. To fabricate In-MoS<sub>2</sub>, the as-collected In-O-MoS<sub>2</sub> powder was subjected to a sulfur vulcanization process in tube furnace to fully remove the lattice oxygen. Typically, 0.3 g sulfur powder (Sinopharm Chemical Reagent Co., Ltd.,  $\geq 99.5\%$ ) and 0.03 g In-O-MoS<sub>2</sub> powders were loaded in the upstream and downstream zones, respectively. The temperature of the tube furnace was raised to 400 °C and kept for 3 h with a heating rate of 5 °C  $\text{min}^{-1}$ . After cooling down to  $25 \pm 2$  °C, the In-MoS<sub>2</sub> powder was obtained. The preparation procedure of pure MoS<sub>2</sub> was the same as that of In-O-MoS<sub>2</sub> in the absence of  $\text{InCl}_3 \cdot 4\text{H}_2\text{O}$ .

**Preparation of In-O-MoS<sub>2</sub>@Ru, In-MoS<sub>2</sub>@Ru.** 0.4 g In-O-MoS<sub>2</sub> powder was uniformly dispersed in 30 mL deionized water, then 0.25 g  $\text{RuCl}_3 \cdot x\text{H}_2\text{O}$  (Aladdin, 35.0–42.0% Ru basis) was added. After continuously stirring for 1 h at room temperature, the solution was moved to an electro-thermostatic water bath heating at 65 °C for 14 h to thoroughly evaporate the water. Afterwards, the dried powder was hand-ground with a mortar and pestle for 0.5 h and transferred to a tube furnace for an annealing procedure at 500 °C for 2 h under H<sub>2</sub>/Ar (10:90) mixture gas with a flow rate of 100 sccm. After cooling down to  $25 \pm 2$  °C, the black product was alternately washed with deionized water and ethyl alcohol for six times, achieving In-O-MoS<sub>2</sub>@Ru. The preparation procedure of In-MoS<sub>2</sub>@Ru was the same as that of In-O-MoS<sub>2</sub>@Ru, except for the precursor is In-MoS<sub>2</sub> powder.

### Material characterization

The crystallographic information and phase components were characterized via powder X-ray diffraction (XRD) measurement using a Rigaku D/Max-KA diffractometer with Cu K $\alpha$  radiation ( $\lambda = 1.5406$  Å). To acquire microstructure information of the samples, the Field emission scanning electron microscope (FE-SEM) was carried out on JSM-7610 F. Transmission electron microscopies (TEM) and high-resolution transmission electron microscopies (HR-TEM) were collected by JEM-2100 (200 kV). High-angle annular dark-field scanning TEM (HAADF-STEM) images were recorded on JEM-ARM 200 F (JEOL, Japan, 200 kV) with a probe spherical aberration corrector to accurately clarify the microstructure at atomic-level. The surface composition and electronic structure information were analyzed by X-ray photoelectron spectroscopy (XPS) equipped by Al K $\alpha$  probe beam (Thermo Scientific K-Alpha). X-ray absorption fine structure (XAFS) spectra embracing X-ray absorption near-edge structure (XANES) and extended X-ray absorption fine structure (EXAFS) of the In, Mo and Ru K-edge were further employed to deeply study the electronic structure information and spatial coordination parameters from the TLS16A1 station (National Synchrotron Radiation Research Center (NSRRC), Taiwan). IFEFFIT software was used for fitting the XAFS results. Fourier transformed infrared (FTIR) spectra was carried out on Perkin Elmer Frontier. Prior to ex situ characterizations, the discharged/charged Li||O<sub>2</sub> cells were disassembled in Ar glove box with H<sub>2</sub>O < 0.1 ppm and O<sub>2</sub> < 0.1 ppm. The used positive electrodes were rinsed with ethylene glycol dimethyl ether (DME, Sinopharm Chemical Reagent Co., Ltd.,  $\geq 99.0\%$ ) to remove the residual electrolyte. Then the positive electrodes were tightly wrapped by protective Parafilm. To ensure the accuracy, they were not taken out of Ar glove box until 10 min. before ex situ characterizations.

### Electrochemical measurements

Typically, the preparation methods of working positive electrodes of Li||O<sub>2</sub> batteries are demonstrated as follows. First, the polytetrafluoroethylene (PTFE) binder (Aladdin, 6 wt.%) was evenly dispersed in isopropyl alcohol solution (Sinopharm Chemical Reagent Co., Ltd.,  $\geq 99.7\%$ ) under magnetic stirring. Then the In-O-MoS<sub>2</sub>@Ru, In-O-MoS<sub>2</sub> and MoS<sub>2</sub> catalysts were homogeneously ground with acetylene black (Hefei Kejing, 99.9%) conductive agent for 0.5 h. Afterwards, the mixed catalysts and acetylene black powders are transferred into the PTFE solution for further magnetic stirring for 12 h. Specially, the mass ratio of the as-fabricated catalysts, PTFE and acetylene black was controlled as 7:1:2. Then, the achieved ink was homogeneously single-side placed onto carbon paper current collector with a diameter of 13 mm (TGP-H-060, Torray, thickness of 0.19 mm, density of 0.44 g  $\text{cm}^{-3}$ ). The active components loadings were controlled as 0.5–0.6 mg  $\text{cm}^{-2}$ . After drying in electric oven at 80 °C for 24 h, the working positive electrode were obtained. To perform a series of electrochemical measurements, 2032 coin cells with 19 holes were assembled in Ar glove box with H<sub>2</sub>O < 0.1 ppm and O<sub>2</sub> < 0.1 ppm. Specifically, the coin cells were comprised of Li foil counter electrode (99.9%, Hefei Kejing, thickness of 0.35 mm, dimension of 13 mm), working positive electrode, glass fiber separator (Whatman, GF/D, thickness of 0.68 mm, dimension of 14 mm), stainless steel spring shim (thickness of 0.2 mm) and LiTFSI/TEGDME electrolyte (1 M, 180  $\mu\text{L}$ ). Prior to cell assembly, all the components were let stand for 24 h in Ar glove box. To ensure even wetting, the electrolyte was slowly dripped onto the GF/D separator by pipette. Prior to measurements, the Li||O<sub>2</sub> cells were left into a custom-built container full of ultra-pure dry O<sub>2</sub> (99.999%, 1.0 atm.) to set for 12 h under  $25 \pm 2$  °C. Then, the galvanostatic discharge/charge procedures were performed on CT2001A LAND multichannel battery testing system. CV testing were carried out on a CHI760E electrochemical workstation with a scanning rate of 0.1 mV  $\text{s}^{-1}$  between 2.0–4.5 V. EIS results were also recorded from a CHI760E workstation applying the amplitude voltage of 5 mV within the frequency range of 10<sup>5</sup> Hz–0.01 Hz. All the electrochemical measurements were conducted under  $25 \pm 2$  °C.

### Computational details

We implemented all DFT calculations by virtue of the CASTEP program with ultrasoft pseudopotentials offered by the Materials Studios package of Accelrys Inc<sup>51</sup>. The Perdew-Burke-Ernzerhof (PBE) functional of generalized gradient approximation (GGA) with the ultrasoft pseudopotentials (USP) were used to describe the electron exchange-correlation potential. The van der Waals interactions were based on the DFT dispersion correction (DFT-D) scheme. A kinetic energy cutoff of 380 eV was used for the smooth parts of the wave functions. The convergence criterions were set to  $5.0 \times 10^{-4}$  eV per atom for energy. The maximum displacement was  $5.0 \times 10^{-4}$  Å and maximum force was 0.01 eV Å, respectively. For the structure optimizations, the Brillouin zone was sampled by a  $2 \times 2 \times 1$  Monkhorst-Pack mesh k-points grid. For the density of states (DOS) calculations, the double k-points meshes were applied. During the course of geometry optimizations, the whole configuration in all the calculations was allowed to relax, which was performed in the reciprocal space. The basal plane of MoS<sub>2</sub> (2H), MoS<sub>2</sub> (1T), In-O-MoS<sub>2</sub>, and In-O-MoS<sub>2</sub>@Ru were modeled by a periodic slab repeated in a  $5 \times 3$  surface unit cell with a vacuum region of 20 Å between the slabs along the z axis. The binding energy of adsorbates O<sub>2</sub>, LiO<sub>2</sub>, and Li<sub>2</sub>O<sub>2</sub> on MoS<sub>2</sub>, In-O-MoS<sub>2</sub>, and In-O-MoS<sub>2</sub>@Ru were calculated by the following equation  $\Delta E_{(\text{ad})} = E_{(\text{surf}+\text{ads})} - E_{(\text{surf})} - E_{(\text{ads})}$ , where the  $E_{(\text{surf}+\text{ads})}$ ,  $E_{(\text{surf})}$ , and  $E_{(\text{ads})}$  are the total energies of the surface covered with and without the adsorbates,  $E_{(\text{ads})}$  is the energy of free O<sub>2</sub>, LiO<sub>2</sub>, or Li<sub>2</sub>O<sub>2</sub> molecules. The optimized structural model is provided in Supplementary Data 1.

## Data availability

All data are available in the main text or the supplementary materials. The source data for Figs and Supplementary Figs generated in this study are provided in the Source Data file. Source data are provided with this paper.

## References

- Bruce, P. G., Freunberger, S. A., Hardwick, L. J. & Tarascon, J.-M. Li-O<sub>2</sub> and Li-S batteries with high energy storage. *Nat. Mater.* **11**, 19–29 (2012).
- Kwak, W.-J. et al. Lithium-oxygen batteries and related systems: potential, status, and future. *Chem. Rev.* **120**, 6626–6683 (2020).
- Li, F. et al. Performance-improved Li-O<sub>2</sub> battery with Ru nanoparticles supported on binder-free multi-walled carbon nanotube paper as cathode. *Energy Environ. Sci.* **7**, 1648–1652 (2014).
- Wang, H. et al. Porous materials applied in nonaqueous Li-O<sub>2</sub> batteries: status and perspectives. *Adv. Mater.* **32**, 2002559 (2020).
- Lv, Q., Zhu, Z., Ni, Y., Geng, J. & Li, F. Spin-state manipulation of two-dimensional metal-organic framework with enhanced metal-oxygen covalency for lithium-oxygen batteries. *Angew. Chem. Inter. Ed.* **61**, e202114293 (2022).
- Feng, N., He, P. & Zhou, H. Critical challenges in rechargeable aprotic Li-O<sub>2</sub> batteries. *Adv. Energy Mater.* **6**, 1502303 (2016).
- Shu, C., Wang, J., Long, J., Liu, H.-K. & Dou, S.-X. Understanding the reaction chemistry during charging in aprotic lithium-oxygen batteries: Existing problems and solutions. *Adv. Mater.* **31**, 1804587 (2019).
- Ma, L. et al. Fundamental understanding and material challenges in rechargeable nonaqueous Li-O<sub>2</sub> batteries: Recent progress and perspective. *Adv. Energy Mater.* **8**, 1800348 (2018).
- Jung, J.-W., Cho, S.-H., Nam, J. S. & Kim, I.-D. Current and future cathode materials for non-aqueous Li-air (O<sub>2</sub>) battery technology-A focused review. *Energy Stor. Mater.* **24**, 512–528 (2020).
- Yang, W. et al. Conversion of intercalated MoO<sub>3</sub> to multi-heteroatoms-doped MoS<sub>2</sub> with high hydrogen evolution activity. *Adv. Mater.* **32**, 2001167 (2020).
- Zang, Y. et al. Tuning orbital orientation endows molybdenum disulfide with exceptional alkaline hydrogen evolution capability. *Nat. Commun.* **10**, 1217 (2019).
- Ma, M. et al. Heterostructures of 2D molybdenum dichalcogenide on 2D nitrogen-doped carbon: superior potassium-ion storage and insight into potassium storage mechanism. *Adv. Mater.* **32**, 2000958 (2020).
- Liu, C., Bai, Y., Zhao, Y., Yao, H. & Pang, H. MoS<sub>2</sub>/graphene composites: fabrication and electrochemical energy storage. *Energy Stor. Mater.* **33**, 470–502 (2020).
- Yang, S.-Z. et al. Rhenium-doped and stabilized MoS<sub>2</sub> atomic layers with basal-plane catalytic activity. *Adv. Mater.* **30**, 1803477 (2018).
- Ji, L. et al. One-pot synthesis of porous 1T-phase MoS<sub>2</sub> integrated with single-atom Cu doping for enhancing electrocatalytic hydrogen evolution reaction. *Appl. Catal. B* **251**, 87–93 (2019).
- Zhang, J., Xu, X., Yang, L., Cheng, D. & Cao, D. Single-atom Ru doping induced phase transition of MoS<sub>2</sub> and S vacancy for hydrogen evolution reaction. *Small Methods* **3**, 1900653 (2019).
- Gao, B. et al. Electron injection induced phase transition of 2H to 1T MoS<sub>2</sub> by cobalt and nickel substitutional doping. *Chem. Eng. J.* **411**, 128567 (2021).
- Jin, Q. et al. H<sub>2</sub>-directing strategy on in situ synthesis of Co-MoS<sub>2</sub> with highly expanded interlayer for elegant HER activity and its mechanism. *Adv. Energy Mater.* **10**, 2000291 (2020).
- Kwon, I. S. et al. Ruthenium nanoparticles on cobalt-doped 1T' phase MoS<sub>2</sub> nanosheets for overall water splitting. *Small* **16**, 2000081 (2020).
- Sun, Y. et al. Plasma-induced large-area N, Pt-doping and phase engineering of MoS<sub>2</sub> nanosheets for alkaline hydrogen evolution. *Energy Environ. Sci.* **15**, 1201–1210 (2022).
- Wang, S. et al. Ultrastable In-plane 1T-2H MoS<sub>2</sub> heterostructures for enhanced hydrogen evolution reaction. *Adv. Energy Mater.* **8**, 1801345 (2018).
- Li, Y. et al. Synergistic Pt doping and phase conversion engineering in two-dimensional MoS<sub>2</sub> for efficient hydrogen evolution. *Nano Energy* **84**, 105898 (2021).
- Lin, H. et al. Simultaneous cobalt and phosphorous doping of MoS<sub>2</sub> for improved catalytic performance on polysulfide conversion in lithium-sulfur batteries. *Adv. Energy Mater.* **9**, 1902096 (2019).
- Cao, D. et al. Engineering the In-plane structure of metallic phase molybdenum disulfide via Co and O dopants toward efficient alkaline hydrogen evolution. *ACS Nano* **13**, 11733–11740 (2019).
- Chen, X. et al. High phase-purity 1T-MoS<sub>2</sub> ultrathin nanosheets by a spatially confined template. *Angew. Chem. Inter. Ed.* **58**, 17621–17624 (2019).
- Li, D. et al. 3D hexapod-shaped Co-ZIFs-S derived Co nanoparticles embedded into nitrogen and sulfur co-doped carbon decorated with ruthenium nanoparticles as efficient catalyst for rechargeable lithium oxygen battery. *Nano Energy* **91**, 106644 (2022).
- Liu, R. et al. Highly efficient electrocatalytic N<sub>2</sub> reduction to ammonia over metallic 1T phase of MoS<sub>2</sub> enabled by active sites separation mechanism. *Adv. Sci.* **9**, 2103583 (2022).
- Qi, K. et al. Single-atom cobalt array bound to distorted 1T MoS<sub>2</sub> with ensemble effect for hydrogen evolution catalysis. *Nat. Commun.* **10**, 5231 (2019).
- Du, Y. et al. The rational doping of P and W in multi-stage catalysts to trigger Pt-like electrocatalytic performance. *J. Mater. Chem. A* **8**, 25165–25172 (2020).
- Strachan, J., Masters, A. F. & Maschmeyer, T. Critical review: hydrothermal synthesis of 1T-MoS<sub>2</sub> - an important route to a promising material. *J. Mater. Chem. A* **9**, 9451–9461 (2021).
- Hou, J. et al. Atomically thin mesoporous In<sub>2</sub>O<sub>3-x</sub>/In<sub>2</sub>S<sub>3</sub> lateral heterostructures enabling robust broadband-light photo-electrochemical water splitting. *Adv. Energy Mater.* **8**, 1701114 (2018).
- Zhou, Y. et al. Lattice-confined Ru clusters with high CO tolerance and activity for the hydrogen oxidation reaction. *Nat. Catal.* **3**, 454–462 (2020).
- Zhu, Y. et al. Single-atom In-doped subnanometer Pt nanowires for simultaneous hydrogen generation and biomass upgrading. *Adv. Funct. Mater.* **30**, 2004310 (2020).
- Zhang, E. et al. Engineering the local atomic environments of indium single-atom catalysts for efficient electrochemical production of hydrogen peroxide. *Angew. Chem. Inter. Ed.* **134**, e202117347 (2022).
- Luo, Z. et al. Band engineering induced conducting 2H-phase MoS<sub>2</sub> by Pd-S-Re sites modification for hydrogen evolution reaction. *Adv. Energy Mater.* **12**, 2103823 (2022).
- Deng, S. et al. Synergistic doping and intercalation: realizing deep phase modulation on MoS<sub>2</sub> arrays for high-efficiency hydrogen evolution reaction. *Angew. Chem. Inter. Ed.* **58**, 16289–16296 (2019).
- Cai, J. et al. Coupling of Ru and O-vacancy on 2D Mo-based electrocatalyst via a solid-phase interface reaction strategy for hydrogen evolution reaction. *Adv. Energy Mater.* **11**, 2100141 (2021).
- Xue, S. et al. Interfacial engineering of lattice coherency at ZnO-ZnS photocatalytic heterojunctions. *Chem. Catal.* **2**, 125–139 (2022).
- Lu, X. et al. Atomic heterointerface boosts the catalytic activity toward oxygen reduction/evolution reaction. *Adv. Energy Mater.* **11**, 2102235 (2021).
- Zhou, Y. et al. Lewis-acidic PtIr multipods enable high-performance Li-O<sub>2</sub> batteries. *Angew. Chem. Inter. Ed.* **60**, 26592–26598 (2021).

41. Li, D. et al. Activating MoS<sub>2</sub> nanoflakes via sulfur defect engineering wrapped on CNTs for stable and efficient Li-O<sub>2</sub> batteries. *Adv. Funct. Mater.* **32**, 2108153 (2022).
42. Xia, Q. et al. MnCo<sub>2</sub>S<sub>4</sub>-CoS<sub>1.097</sub> heterostructure nanotubes as high efficiency cathode catalysts for stable and long-life lithium-oxygen batteries under high current conditions. *Adv. Sci.* **8**, 2103302 (2021).
43. Ganapathy, S. et al. Use of nano seed crystals to control peroxide morphology in a nonaqueous Li-O<sub>2</sub> battery. *J. Phys. Chem. C* **120**, 18421–18427 (2016).
44. Jaradat, A. et al. High performance air breathing flexible lithium-air battery. *Small* **17**, 2102072 (2021).
45. Yang, T. et al. In situ imaging electrocatalytic CO<sub>2</sub> reduction and evolution reactions in all-solid-state Li-CO<sub>2</sub> nanobatteries. *Nanoscale* **12**, 23967–23974 (2020).
46. Tian, F., Radin, M. D. & Siegel, D. J. Enhanced charge transport in amorphous Li<sub>2</sub>O<sub>2</sub>. *Chem. Mater.* **26**, 2952–2959 (2014).
47. Yang, Y. et al. Tuning the morphology and crystal structure of Li<sub>2</sub>O<sub>2</sub>: a graphene model electrode study for Li-O<sub>2</sub> battery. *ACS Appl. Mater. Inter.* **8**, 21350–21357 (2016).
48. Chen, K. et al. The stabilization effect of CO<sub>2</sub> in lithium-oxygen/CO<sub>2</sub> batteries. *Angew. Chem. Inter. Ed.* **59**, 16661–16667 (2020).
49. Chen, L.-B. et al. Effects of CO<sub>2</sub> accumulation during cycling of a Li-O<sub>2</sub> battery on the transition of discharge product and performance fading. *Nano Energy* **66**, 104171 (2019).
50. Jiang, Y. et al. Mildly oxidized MXENE (Ti<sub>3</sub>C<sub>2</sub>, Nb<sub>2</sub>C, and V<sub>2</sub>C) electrocatalyst via a generic strategy enables longevous Li-O<sub>2</sub> battery under a high rate. *ACS Nano* **15**, 19640–19650 (2021).
51. Clark, S. J. et al. First principles methods using CASTEP. *Z. Kristallogr. Cryst. Mater.* **220**, 567–570 (2005).

## Acknowledgements

The authors acknowledge support from the project supported by the State Key Program of National Natural Science of China (No. U1906227, L. Y.), and Taishan Pandeng Project of Shandong Province (L. Y.).

## Author contributions

L.Y. initiated and directed the study. P.W. performed the experiment and completed the manuscript. D.Z., P.Z., and X.H. helped with the electrochemical performance measurement, the XAFS, and HAADF-STEM analysis. Z.Z. and R.W. assisted in schematic illustrations of the working mechanism of the catalysts. C.W. contributed to the data analyzes and discussions. X.L. conducted the DFT calculations. X.G. and Y.C.L. helped

with the experiment design, result evaluation and manuscript revise. All authors contributed to the discussion and revising of this manuscript.

## Competing interests

The authors declare no competing interests.

## Additional information

**Supplementary information** The online version contains supplementary material available at <https://doi.org/10.1038/s41467-024-55073-5>.

**Correspondence** and requests for materials should be addressed to Zhiwei Zhang, Rutao Wang, Xiaoli Ge, Xiaojing Liu or Longwei Yin.

**Peer review information** *Nature Communications* thanks Chun Yuen Kwok, and the other, anonymous, reviewers for their contribution to the peer review of this work. A peer review file is available.

**Reprints and permissions information** is available at <http://www.nature.com/reprints>

**Publisher's note** Springer Nature remains neutral with regard to jurisdictional claims in published maps and institutional affiliations.

**Open Access** This article is licensed under a Creative Commons Attribution-NonCommercial-NoDerivatives 4.0 International License, which permits any non-commercial use, sharing, distribution and reproduction in any medium or format, as long as you give appropriate credit to the original author(s) and the source, provide a link to the Creative Commons licence, and indicate if you modified the licensed material. You do not have permission under this licence to share adapted material derived from this article or parts of it. The images or other third party material in this article are included in the article's Creative Commons licence, unless indicated otherwise in a credit line to the material. If material is not included in the article's Creative Commons licence and your intended use is not permitted by statutory regulation or exceeds the permitted use, you will need to obtain permission directly from the copyright holder. To view a copy of this licence, visit <http://creativecommons.org/licenses/by-nc-nd/4.0/>.

© The Author(s) 2025